Cell Reports

Report

Spatial proteomics identifies a CRTC-dependent viral signaling pathway that stimulates production of interleukin-11

Graphical abstract

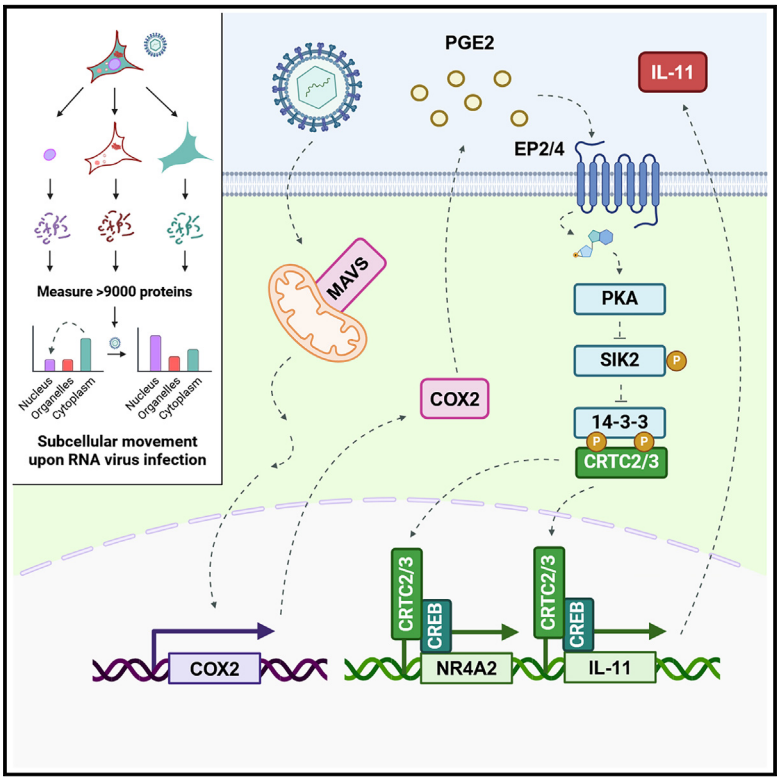

Authors

Benjamin J. Ravenhill, Marisa Oliveira, George Wood, ..., Betty Chung, Georg H.H. Borner, Michael P. Weekes

Correspondence

mpw1001@cam.ac.uk

In brief

Ravenhill et al. employ subcellular proteomics to quantify the movement of >9,000 proteins during infection with the model RNA virus Sendai. In addition to known controls, CRTC2 and CRTC3 translocate to the nucleus, triggering a transcriptional program that includes profibrogenic cytokine IL-11 and antiviral factor NR4A2.

Highlights

- Proteomic translocation analysis of 9,100 proteins during infection with model RNA virus
- CREB-regulated transcription coactivators 2 and 3 translocate to the nucleus in infection
- Relocalization is dependent on MAVS, cyclo-oxygenase proteins, and protein kinase A
- Nuclear CRTC2/3 trigger transcription of profibrogenic cytokine IL-11 and antiviral NR4A2

Ravenhill et al., 2025, Cell Reports *44*, 115263
February 25, 2025
https://doi.org/10.1016/j.celrep.2025.115263

CellPress

Cell Reports

CellPress
OPEN ACCESS

Report

Spatial proteomics identifies a CRTC-dependent viral signaling pathway that stimulates production of interleukin-11

Benjamin J. Ravenhill,[1,2,9] Marisa Oliveira,[1,2,9] George Wood,[3] Ying Di,[1,2] Joanne Kite,[1,2] Xinyue Wang,[1,2] Colin T.R. Davies,[1,2] Yongxu Lu,[4] Robin Antrobus,[1,2] Gill Elliott,[5] Nerea Irigoyen,[3] David J. Hughes,[6] Paul A. Lyons,[2,7] Betty Chung,[3] Georg H.H. Borner,[8,10] and Michael P. Weekes[1,2,10,11,*]

[1]Cambridge Institute for Medical Research, University of Cambridge, Cambridge, UK
[2]Department of Medicine, University of Cambridge, Cambridge, UK
[3]Department of Pathology, University of Cambridge, Cambridge, UK
[4]Sir William Dunn School of Pathology, University of Oxford, Oxford, UK
[5]Department of Microbial Sciences, School of Biosciences, University of Surrey, Guildford, UK
[6]School of Biology, University of St. Andrews, St. Andrews, UK
[7]Cambridge Institute of Therapeutic Immunology and Infectious Disease, Jeffrey Cheah Biomedical Centre, University of Cambridge, Cambridge, UK
[8]Max Planck Institute of Biochemistry, Am Klopferspitz 18, Martinsried, Germany
[9]These authors contributed equally
[10]Senior author
[11]Lead contact
*Correspondence: mpw1001@cam.ac.uk
https://doi.org/10.1016/j.celrep.2025.115263

SUMMARY

Appropriate cellular recognition of viruses is essential for the generation of an effective innate and adaptive immune response. Viral sensors and their downstream signaling components thus provide a crucial first line of host defense. Many of them exhibit subcellular relocalization upon activation, resulting in the expression of interferon and antiviral genes. To comprehensively identify signaling factors, we analyzed protein relocalization on a global scale during viral infection. cAMP-responsive element-binding protein (CREB)-regulated transcription coactivators 2 and 3 (CRTC2/3) exhibited early cytoplasmic-to-nuclear translocation upon infection with multiple viruses in diverse cell types. This movement was dependent on mitochondrial antiviral signaling protein (MAVS), cyclo-oxygenase proteins, and protein kinase A. A key effect of CRTC2/3 translocation is transcription of the fibro-inflammatory cytokine interleukin (IL)-11. This may be important clinically in viral infections associated with fibrosis, including SARS-CoV-2. Nuclear translocation of CRTC2/3 is, therefore, identified as an important pathway in the context of viral infection.

INTRODUCTION

Subcellular relocation of cellular sensors and their signaling components forms a crucial first step in the recognition of any intracellular pathogen and determines the outcome of infection by orchestrating effective antiviral immunity. For example, known RNA sensor RIG-I translocates upon activation to mitochondrial antiviral signaling protein (MAVS) on the outer mitochondrial membrane and mitochondria-associated membrane (MAM).[1] Cyclic GMP-AMP synthase (cGAS) and other sensors recognize cytosolic viral DNA, resulting in the endoplasmic reticulum (ER)-to-Golgi transition of stimulator of interferon genes (STING).[2,3] Activation of these sensors leads to intermediate signaling and nuclear translocation of terminal signaling components IRF3 and nuclear factor κB (NF-κB), triggering the production of interferon (IFN) and the synthesis of IFN-stimulated genes (ISGs), including proteins limiting viral replication.[4–6]

IRF3 and NF-κB are critical final common mediators for viral, bacterial, fungal, and parasitic sensing pathways.[7,8] Systematic mapping of analogous, novel signaling pathways will, therefore, provide fundamental new insights into intrinsic immunity and transform our understanding of how pathogen recognition triggers immune gene expression. A detailed mechanistic understanding of known sensing/signaling components has led directly to (1) the development of vaccine adjuvants, (2) insights into autoimmune disease, and (3) treatments for chronic inflammation and cancer.[9–12]

We hypothesized that novel terminal signaling molecules would share the characteristic of subcellular redistribution. To identify these components on a global scale, we employed proteomic "subcellular profiling"[13–15] to globally quantify subcellular protein redistribution in cells infected with the model RNA virus Sendai, which is a particularly potent RIG-I agonist due to the production of defective-interfering RNAs.[16,17]

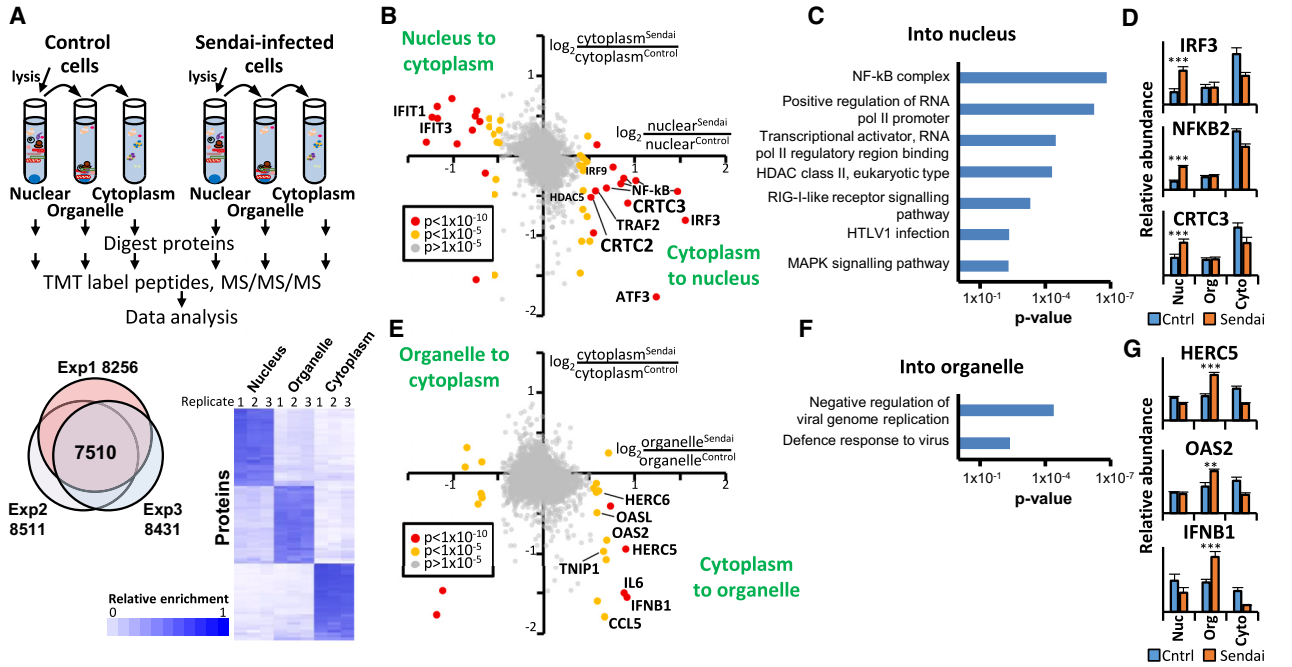

Figure 1. Subcellular profiling during Sendai infection identifies translocation of CRTC2 and CRTC3 from cytoplasm to nucleus

(A) Top: schematic of the experiment. Differential centrifugation of mechanical cellular lysates separated nuclear and organellar fractions, with the supernatant as the cytoplasmic fraction. Bottom: overlap of proteins quantified in each replicate experiment and hierarchical clustering analysis of markers of each fraction (Table S3)

(B) Scatterplot of nucleocytoplasmic movement of proteins quantified in all three replicates (8 h infection with Sendai virus or control, $n = 3$). Benjamini-Hochberg-corrected significance A values[19] were used to estimate p values for the nuclear Sendai/nuclear control ratio, and the dots are colored according these values. The fold change for cytoplasmic movement was, in some cases, small, which may reflect a relatively large initial cytoplasmic protein pool.

(C) Functional enrichment analysis of proteins moving in to the nucleus with $p < 1 \times 10^{-5}$ (see also Table S2C).

(D) Example results. Error bars: SEM. p values calculated for (B) are shown: $^{***}p < 1 \times 10^{-10}$.

(E) Scatterplot of organelle-cytoplasmic movement as described in (B).

(F) Functional enrichment analysis of proteins moving in to organelles with $p < 1 \times 10^{-5}$ (see also Table S2E).

(G) Example results. Error bars: SEM. p values calculated for (E) are shown: $^{**}p < 1 \times 10^{-5}$ and $^{***}p < 1 \times 10^{-10}$.

RESULTS

Subcellular profiling identifies nucleocytoplasmic translocation of CRTC2 and CRTC3 during Sendai virus infection of human fibroblasts

Subcellular profiling (Figure 1A) can both identify subcellular protein location and give unbiased information about protein movement upon any stimulus.[13,14] We chose to infect human telomerase reverse transcriptase (hTERT) immortalized primary human fetal foreskin fibroblasts (HFFF-TERTs) since we have previously performed extensive proteomic characterization of these cells, identifying their expression of a full complement of sensing and signaling proteins and characterizing an essentially identical response to infection as their non-immortalized primary equivalents.[18] Since overall changes in protein abundance may affect movement calculations, 8 h of infection with Sendai virus was studied, where only 87/8,540 (1.0%) of human proteins were induced, on average, by >2-fold. At this time point, the nuclear translocation of our positive control, IRF3, was also maximal, suggesting that sensitivity for the detection of other organellar protein transitions would be optimal (Figures S1A–S1E; Tables S1, S2A, and S2B).

Subcellular profiling quantified 9,176 human proteins and 8 Sendai proteins in total, with 7,510 human proteins quantified in all three biological replicates (Figure 1A). An interactive spreadsheet of all proteomic data in this manuscript is provided in Table S1, enabling graphical visualization of each quantified protein. The locations of known marker proteins from each organelle were discriminated well (Figures 1A; Table S3). The redistribution of IRF3 and five Rel-like domain-containing proteins of the NF-κB family validated our approach, and DAVID functional enrichment analysis of proteins moving into the nucleus indicated that a variety of transcriptional regulators and components of known antiviral signaling pathways exhibited redistribution upon infection (Figures 1B–1D; Table S2C). cAMP-responsive element-binding protein (CREB)-regulated transcription coactivators 2 and 3 (CRTC2/3) were both among the proteins exhibiting the greatest degree of cytoplasmic-nuclear translocation (Figures 1B–1D; Table S2C). Activating transcription factor 3 (ATF3), which is a CREB-family transcription factor with a range of cellular effects, including on NF-κB signaling and inflammation, also showed a high degree of nucleocytoplasmic redistribution.[20,21] Unlike CRTC2/3, ATF3 was significantly induced following Sendai virus infection, which

may confound apparent movement (Figure S1F). Proteins redistributing from the cytoplasm to the nucleus also included the class IIa histone deacetylases (HDACs) 4, 5, and 7; we have previously shown that HDAC4 and -5 can restrict infection by DNA viruses, including herpes simplex virus 1 (HSV1) and vaccinia virus.[22,23] Oxysterol-binding protein-like 3 (OSBPL3) moved from cytosol to organelles, in keeping with a role in remodeling membranes following stimulation.[24]

Cytosol-to-nuclear translocation of IRF9 suggested that by 8 h of infection, type I IFN signaling was occurring.[25] Indeed, a number of proteins appeared to move out of the nucleus into the cytoplasm (Figure 1B, top left; Table S2D), of which 19/22 were ISGs (Interferome 2.01[26]), and 15/22 were upregulated >1.5-fold during the Sendai virus time-course analysis (Figure S1G; Tables S1 and S2D). This suggests that the observed nuclear-cytoplasmic movement might rather reflect increased cytosolic protein synthesis (or indeed both protein synthesis and movement). Proteins seemingly redistributing from the cytoplasm to the organelle were also enriched in antiviral functions, including oligoadenylate synthetase 2 (OAS2), 2′-5′-OAS-like (OASL), and HECT and RLD domain containing E3 ubiquitin protein ligases 5 and 6 (HERC5/6) (Figures 1E–1G; Table S2E), although this could again represent *de novo* synthesis. Several proteins also appeared to move between organelles and the nucleus following infection, including ATF3, although as discussed above, this may also be due to increased translation of a nuclear-resident protein (Figures S1H and S1I).

Early nucleocytoplasmic translocation of CRTC2 and CRTC3 during infection with diverse viruses and in diverse cell types

We confirmed that both ectopically expressed and endogenous CRTC2 and CRTC3 relocated from the cytoplasm to the nucleus upon Sendai infection by immunofluorescence microscopy (Figures 2A, 2B, and S3A). Cells with translocating CRTC2 largely also translocated CRTC3 (Figure 2C). To determine whether our findings were limited to the infection of fibroblasts by Sendai virus or represented a more general response to viral infection, we firstly examined other RNA viruses or equivalent stimuli. CRTC2 and CRTC3 both exhibited nucleocytoplasmic relocation upon lipofection with poly(I:C) (PIC) (Figures 2D and 2E) and infection with respiratory syncytial virus (RSV) (Figures 2F and S2A). Importantly, infection with DNA viruses or equivalent stimuli also led to CRTC2/3 translocation, including calf thymus DNA (CT-DNA), modified vaccinia Ankara (MVA), HSV1, and human cytomegalovirus (HCMV) infection (Figures 2G and S2B–S2D).

CRTC2 also translocated into the nucleus during Sendai virus infection of A549 cells, human umbilical vein endothelial cells (HUVECs), and HBEC3-KT lung epithelial cells.[27] However, in these cells, CRTC3 exhibited a predominantly nuclear localization prior to infection, although there was a small yet significant increase in nuclear CRTC3 upon infection of HUVECs and A549 cells (Figures S3B–S3D). Based on immunofluorescence microscopy data, it appears that each cell line has a different basal level of CRTC2 and CRTC3 in the nucleus. To determine the kinetics of CRTC2/3 translocation, we infected HFFF-TERT cells stably expressing hemagglutinin (HA)-tagged CRTC2/3 with Sendai virus. CRTC3 accumulated in nuclei between 2 and 4 h post-infection, whereas CRTC2 did not start to translocate until 4–6 h (Figure 2H). The response of CRTC2/3 to multiple stimuli in diverse cell types suggests that this is an important pathway in the context of viral infection.

CRTC2 and CRTC3 are required for transcription of a distinct subset of genes in response to viral infection

CRTC2/3 proteins are members of a family of transcriptional co-activators of CREB, originally identified as interleukin (IL)-8 activating proteins.[28] CRTC nuclear translocation is an essential, conserved step in the activation of a subset of cAMP-responsive genes (Figure 3A), with key regulatory roles in energy homeostasis, long-term memory, and longevity.[29] CRTC-associated enhancement of CREB-dependent transcription appears to be independent of, but synergistic with, CREB S133 phosphorylation.[30] In basal conditions, CRTC2 and CRTC3 are held in the cytosol by their phospho-specific interactions with 14-3-3 proteins[31] and, following dephosphorylation, translocate to the nucleus to act as coactivators.[32]

To determine the effects of CRTC2/3 in the context of viral infection, RNA sequencing (RNA-seq) was used to analyze cells depleted of both proteins, then they were infected with Sendai virus (Figures 3B and S5A). The gene most significantly downregulated in the absence of CRTC2/3 was IL-11. Interestingly, IL-11 has recently been implicated in fibro-inflammatory processes[33–36] and has previously been shown to be released in response to viral infection via an undefined axis.[37–39] Supporting our results, one of the next most significantly differentially regulated transcripts was nerve growth factor IB-like receptor NR4A2 (also known as Nurr1), which has previously been characterized as a CRTC-dependent gene and shown to silence HIV gene expression during infection.[30,40,41] Expression of IL-11 and NR4A2 in a CRTC2- and CRTC3-dependent manner was validated by RT-qPCR and ELISA for IL-11 (Figure 3C).

Given that CRTC2 and CRTC3 are from the same family of proteins, we next sought to test whether their role was redundant. Single CRTC2 and CRTC3 knockout cell lines (CRTC2 KO and CRTC3 KO) and a double KO cell line (CRTC2/3 DKO) were generated and then either complemented with the wild-type construct, a mutant lacking the N-terminal 50 amino acids (the CREB binding domain for both CRTC2 and CRTC3), or a vector-only control. After infection with Sendai virus, the transcripts were sequenced (Figures 3D, 3E, and S4A–S4C; Table S5). In CRTC2-KO and CRTC3-KO cells complemented with the vector or their respective wild-type gene, IL-11 and NR4A2 were two of the most significantly differentially expressed genes (Figure 3D). This occurred despite residual expression of the other CRTC in the single KO cells. We suspect that this may be a consequence of overexpression and note that a replacement of either CRTC2 or CRTC3 alone in CRTC2/3 DKO cells was sufficient to result in a similar transcriptional profile to double-complemented cells (Figures S5C, S4D, and S4E). CRTC2/3 function was dependent on the CREB-binding N terminus of the proteins, as transcription was similar in CRTC2-KO or CRTC3-KO cells complemented

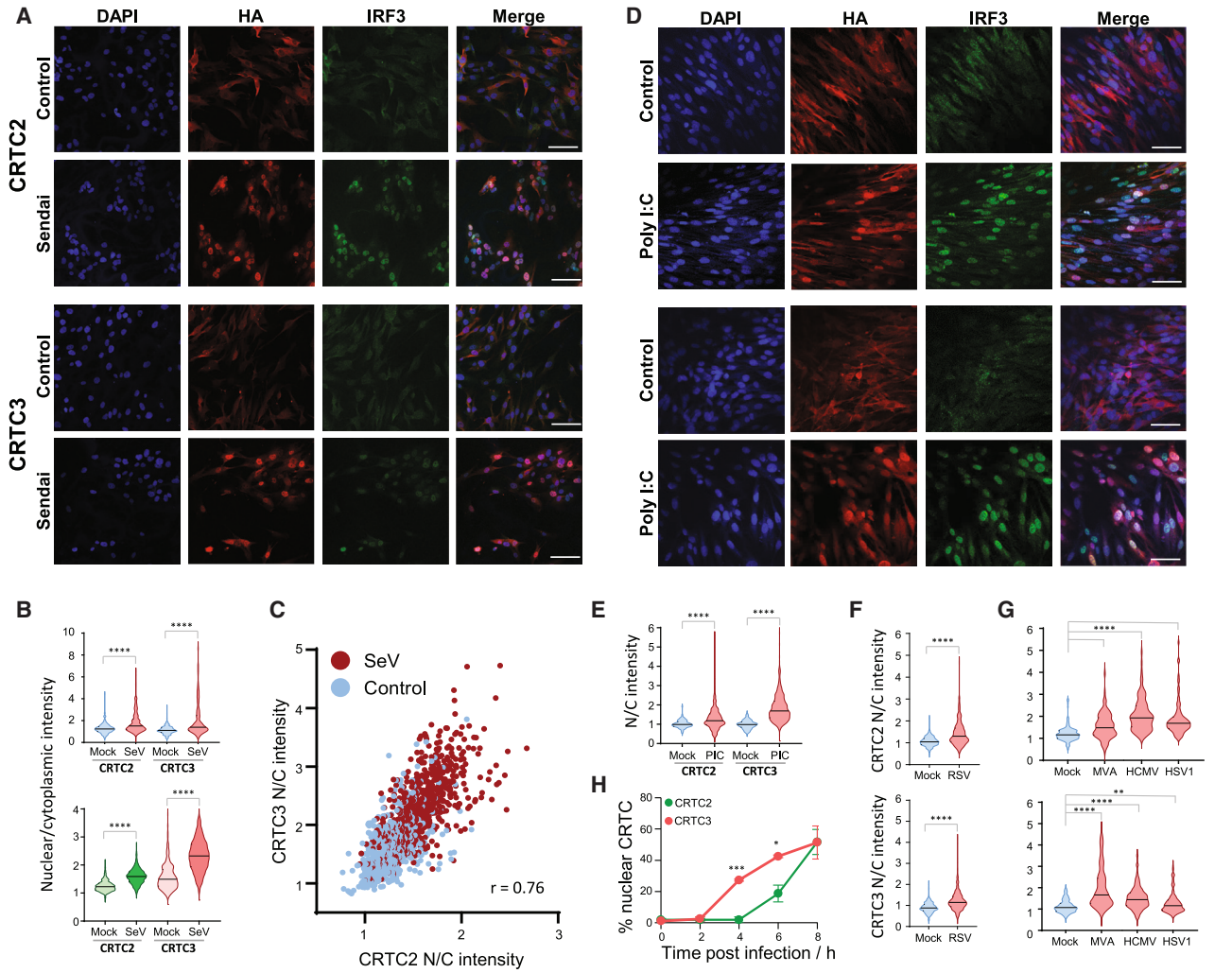

Figure 2. CRTC2 and CRTC3 translocate from cytoplasm to nucleus in response to infection with diverse viruses

(A) Representative immunofluorescence analysis of nucleocytoplasmic movement of HA-tagged CRTC2 and CRTC3 and endogenous IRF3 after 8 h of infection with Sendai virus or control. Translocation of endogenous CRTC2/3 is shown in Figure S3A. In infected cells compared to controls, IRF3 staining appeared brighter upon nuclear relocation; however, as IRF3 was not induced (Figure S1F), this is likely to represent the concentration in a smaller compartment.

(B) Top: quantitation of movement shown in (A); bottom: quantitation of endogenous CRTC2/3 nuclear/cytoplasmic intensity after 8 h of Sendai virus infection or control treatment (representative images shown in Figure S3A). CellProfiler was used for quantitation (STAR Methods). Briefly, nuclei were defined by the area of DAPI staining. Cytosol was defined by extending the area of the nuclear mask by 10 pixels and then subtracting the area covered by the nuclear mask. A nuclear:cytoplasmic (N:C) ratio was calculated. For this and subsequent subfigures, a minimum of 80 cells were quantified. ****$p < 0.0001$.

(C) Correlation of CRTC2/3 translocation from cytoplasm to nucleus after Sendai virus infection (8 h). Pearson r = 0.7599 (95% confidence interval: 0.7351–0.7826). Two-tailed p-value <0.0001.

(D) Representative immunofluorescence analysis 8 h post lipofection with poly I:C (4 μg/mL).

(E) Quantitation of movement shown in (D). ****$p < 0.0001$.

(F) Quantitation of movement upon RSV infection from Figure S2A.

(G) Quantitation of movement upon MVA, HCMV, and HSV-1 infection from Figures S2C and S2D. **$p < 0.01$ and ****$p < 0.0001$.

(H) Temporal kinetics of nuclear translocation of stably overexpressed CRTC2 and CRTC3. $n = 3$, counting at least 100 nuclei per replicate over at least two fields. Error bars: SEM. *$p < 0.05$ and ***$p < 0.0005$. Scale bar: 100 μm.

with control or the respective ΔN50 CRTC (Figure 3E). We confirmed that complementation of either CRTC2 or CRTC3 KOs with their respective wild type, but not ΔN50 CRTC2 or ΔN50 CRTC3, was sufficient to enhance the transcription of IL-11 and NR4A2 (Figure 3F). Together, these data strongly suggest that CRTC2 and CRTC3 target the same subset of cellular promoters in response to infection. Analysis of the promoters of CRTC2/3-regulated genes revealed an enrichment of the motif 5'-CGGTGACGTCAGC-3', which contains the CREB1 consensus motif of 5′-TGACGTCA-3′, again supporting the role of CREB in the actions of CRTC2 and CRTC3 (Figure S5D; Table S4).

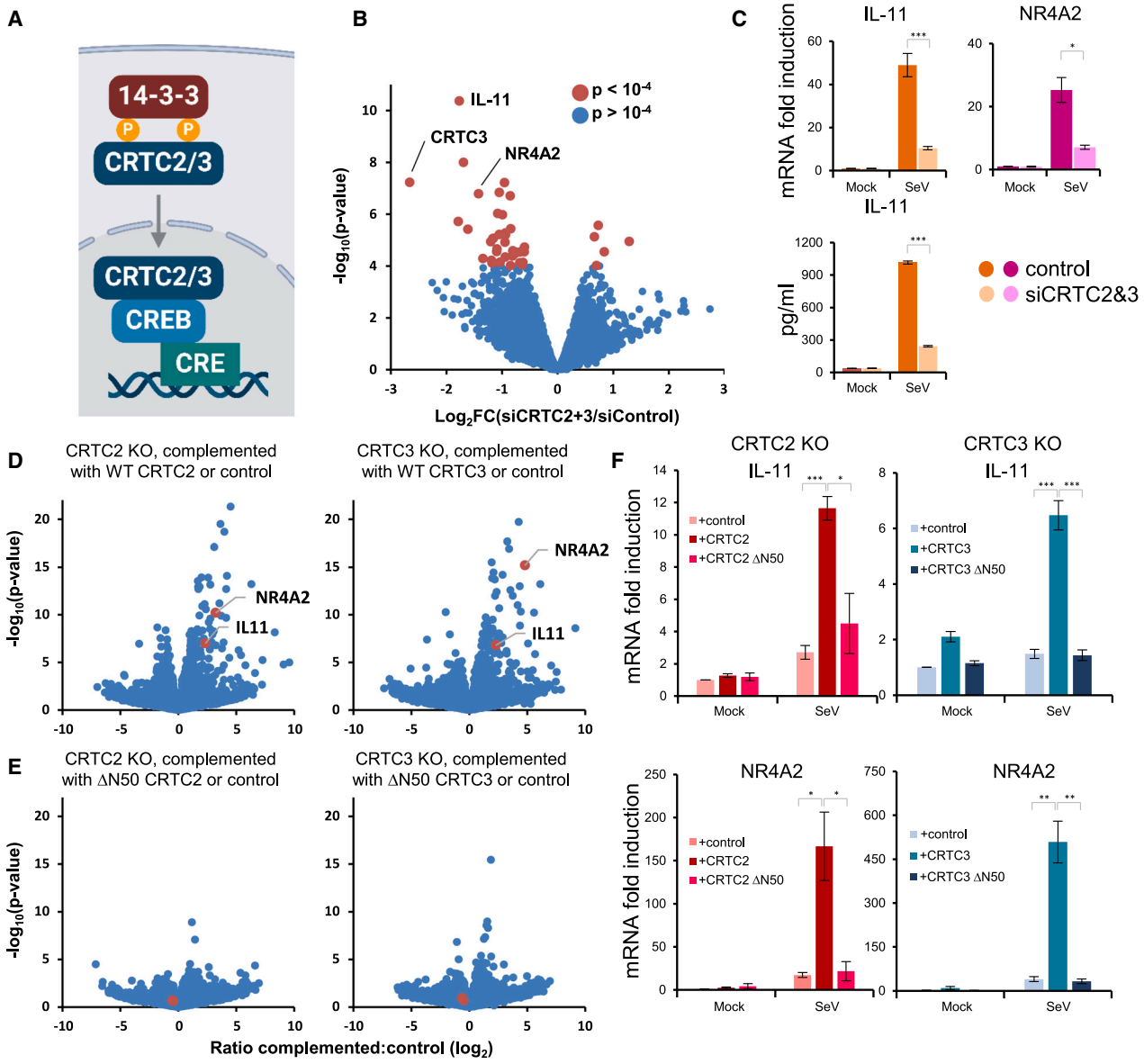

Figure 3. Function of CRTC2 and CRTC3 in viral infection

(A) Regulation and function of CRTC molecules. Under basal conditions, CRTCs are phosphorylated at conserved sites and sequestered in the cytoplasm through interactions with 14-3-3 proteins. Dephosphorylated CRTCs translocate to the nucleus, where they bind CREB, stimulating transcriptional activation of cAMP-responsive element (CRE)-containing target genes. CRTCs all include a CREB-binding domain (CBD), a regulatory region (RR), and a transactivation domain (TAD).

(B) RNA-seq comparing HFFF-TERTs knocked down for both CRTC2 and CRTC3 or control and then infected with Sendai virus for 8 h. $n = 3$. CRTC2 was not reliably quantified, but depletion was confirmed by qPCR (Figure S5A). FC, fold change.

(C) CRTC-dependent induction of IL-11 and NR4A2 in cells knocked down for both CRTC2 and CRTC3 or control and then infected with Sendai virus. Top: qPCR analysis for IL-11 ($n = 4$, 24 h infection) and NR4A2 ($n = 3$, 8 h infection). Bottom: ELISA of IL-11 in cellular supernatant following 24 h infection with Sendai virus or control. $n = 4$. Error bars: SEM.

(D and E) Volcano plots showing differential transcript expression by RNA-seq in cells singly knocked out for CRTC2 or CRTC3, complemented with the respective wild-type or ΔN50 gene or control and then infected with Sendai (8 h). $n = 3$.

(F) qPCR to validate findings in (E) for IL-11 and NR4A2. CRTC2, $n = 3$, 8 h infection; CRTC3, $n = 4$, 8 h infection. Error bars: SEM. $^{*}p < 0.05$, $^{**}p < 0.01$, and $^{***}p < 0.001$.

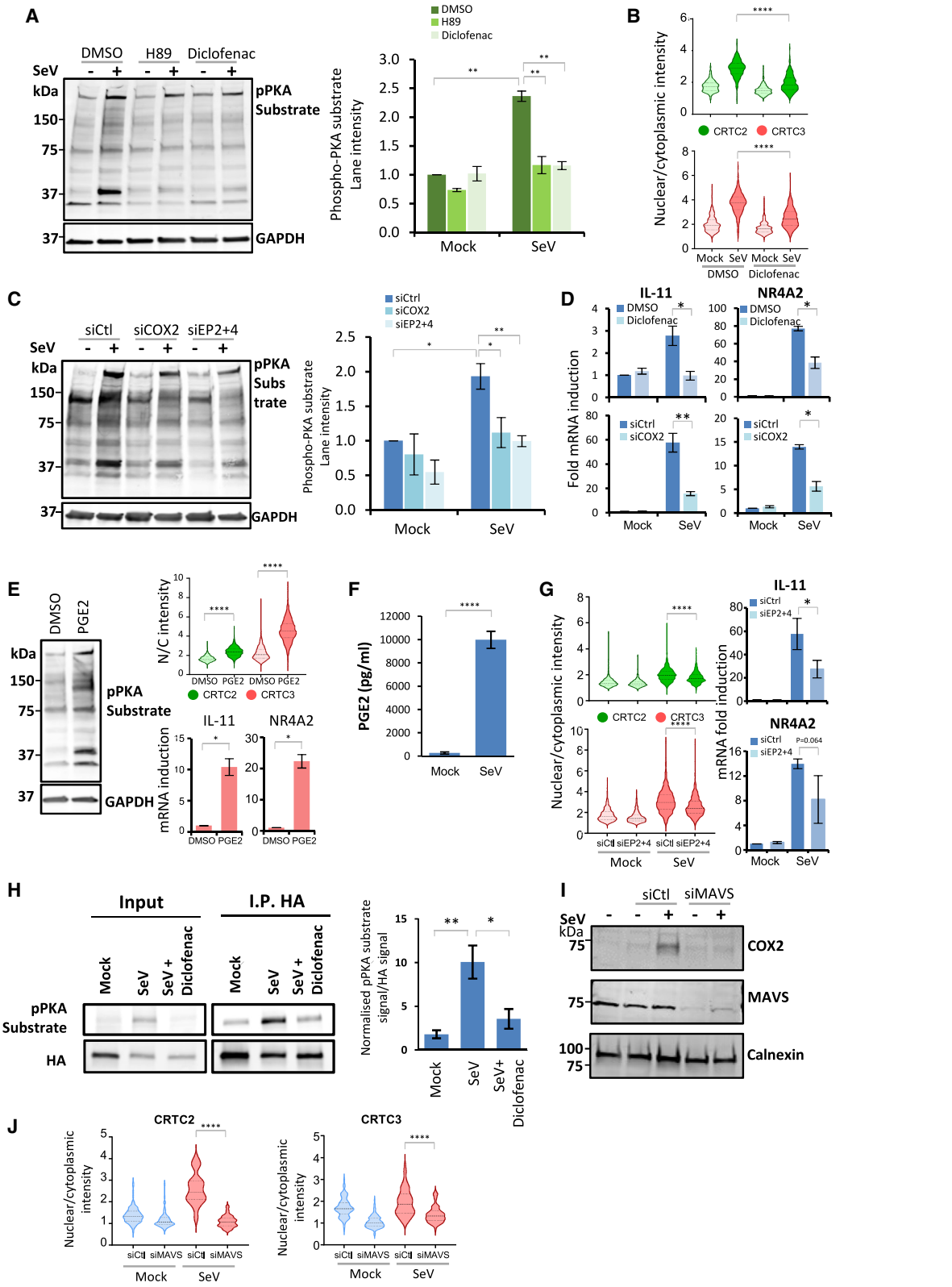

(legend on next page)

Nuclear translocation of CRTC2 and CRTC3 during infection is dependent on MAVS, COX2, and PKA

Given the surprising observation that both RNA and DNA stimuli were capable of inducing CRTC2 and CRTC3 nuclear translocation, we attempted to identify the pathway through which this movement was triggered. Upon other types of stimulus, CRTC2 and CRTC3, in addition to HDAC4 and -5 (Figure 1B), translocate into the nucleus following cAMP/protein kinase A (PKA) signaling.[31,42,43] Both CRTC2 and CRTC3 are phosphorylated by protein kinase SIK2[44,45] at sites that enhance their interaction with 14-3-3 proteins. In response to the activation of PKA by cAMP, SIK2 itself is phosphorylated and its kinase activity toward CRTC2 and CRTC3 reduced, allowing their release from 14-3-3 proteins and translocation to the nucleus. We therefore assessed whether the cAMP signaling pathway was activated during Sendai infection. PKA is a canonical effector of cAMP signaling, and immunoblot using a pan-phospho-PKA substrate antibody demonstrated an increase in PKA substrate phosphorylation in Sendai-infected cells, which was inhibited by the PKA inhibitor H89 (Figure 4A).

Many cell surface receptors are coupled to adenylyl cyclase, but relatively few are linked to infection or inflammation. Conversely, elevation of cyclo-oxygenase 2 (COX2; also known as prostaglandin-endoperoxide synthase 2 [PTGS2]) is a well-established component of the inflammatory response, which is induced in infection.[46,47] This results in elevated levels of prostaglandins driving pyrexia and inflammation.[48,49] Our proteomic analysis demonstrated that COX2, but not COX1, was induced in response to Sendai (Figure S6B). Blocking both COX1 and COX2 with the non-steroidal anti-inflammatory drug diclofenac not only resulted in a reduction in PKA activity in the context of Sendai virus infection but also significantly reduced the nuclear translocation of CRTC2 and CRTC3 and the transcription of IL-11 and NR4A2. The knockdown of COX2 also reduced the transcription of IL-11 and NR4A2 (Figures 4A–4D and S6C).

COXs catalyze the production of prostaglandins, and prostaglandin E2 (PGE2) has previously been shown to induce the translocation of CRTC proteins.[50] We confirmed secretion of PGE2 following Sendai virus infection by ELISA and that PGE2 treatment induced PKA activation, CRTC2 and CRTC3 translocation, and IL-11 and NR4A2 transcription in our system (Figures 4E, 4F, and S6D). PGE2 signals via four known receptors, EP1–4, of which EP2 and EP4 positively signal via the adenylyl-cyclase-PKA pathway[51] and are expressed in HFFF-TERTs from our RNA-seq data (Table S5). Depletion of EP2 and EP4 by small interfering RNA (siRNA) was sufficient to impair Sendai virus infection-induced activation of PKA, nuclear translocation of CRTC2 and CRTC3, and transcription of IL-11 (Figures 4C, 4G, and S4G). Consistent with SIK2 acting downstream of PKA following activation by PGE2,[50] we found that SIK2 was phosphorylated at PKA target residues in response to Sendai virus infection. Furthermore, this was reversed by diclofenac treatment, in keeping with a COX-dependent signaling event (Figure 4H).

MAVS is a core component of the cellular response to RNA virus infection and is required for downstream activation of IRF3 and NF-κB.[4] As the COX2 promoter contains an NF-κB response element,[52] we tested whether MAVS depletion could similarly impair this pathway. Knockdown of MAVS led to a failure to induce COX2 at the protein level in response to Sendai virus infection and, similarly, led to a defect in CRTC2/3 nuclear import (Figures 4I and 4J). The knockdown of MAVS also led to a defect in CRTC2/3 nuclear import in response to infection with MVA, a DNA virus (Figure S7). It remains to be determined whether this is also dependent on RIG-I; however, it is not without precedent for a DNA stimulus to trigger signaling via

Figure 4. Virus-induced translocation of CRTC2 and CRTC3 is MAVS, COX2, and PKA dependent

(A) Immunoblot showing an increase in PKA substrate phosphorylation following Sendai virus infection. HFFF-TERTs were treated with DMSO, PKA inhibitor H89 (20 μM), and COX1/COX2 inhibitor diclofenac (20 μM) for the final 6 h of an 8 h infection with Sendai virus. Pan-phospho-PKA (pPKA) substrate and GAPDH signal were analyzed; quantitation is to the right ($n = 3$). Error bars: SEM.

(B) Reduced nuclear translocation of endogenous CRTC2 and CRTC3 upon COX inhibition by diclofenac during Sendai virus infection (8 h) of HFFF-TERTs. For this and subsequent similar subfigures, a minimum of 200 cells were quantified in each of $n = 3$ experiments as described in Figure 2B and STAR Methods. Data are representative of three experiments.

(C) Immunoblot showing an increase in PKA substrate phosphorylation following Sendai virus infection, which is COX2 and EP2 and -4 dependent. HFFF-TERTs were transfected with siRNAs targeting COX2 or EP2 and -4 72 h prior to 8 h infection with Sendai virus. pPKA substrate and GAPDH signal were analyzed; quantitation is to the right ($n = 3$). Error bars: SD.

(D) Reduced transcription of IL-11 and NR4A2 in Sendai virus-infected cells following depletion of COX2 (24 h infection) or treatment with 20 μM diclofenac (8 h infection). $n = 3$ (IL-11) or 4 (NR4A2). Plotted values represent the average ± SEM.

(E) Representative immunoblot (left, $n = 3$), quantitative immunofluorescence (right, top, $n = 3$), and qPCR (right, bottom, $n = 3$) demonstrating that PGE2 (20 μM, 6 h) stimulates activation of PKA and nuclear translocation of CRTC2 and CRTC3 in HFFF-TERT cells while also stimulating transcription of IL-11 and NR4A2. Quantitation of the immunoblots is shown in Figure S6A. Representative immunofluorescence images are shown in Figure S6D.

(F) Release of PGE2 in supernatants from cells infected with Sendai virus for 24 h. The control siRNA-treated supernatants from Figure 3C were analyzed by PGE2-specific ELISA. $n = 4$. Error bars: SD.

(G) Quantitative immunofluorescence ($n = 3$) and qPCR ($n = 3$) demonstrating that siRNA depletion of EP2 and EP4 impairs Sendai virus-induced nuclear translocation of CRTC2 and CRTC3 (left) and IL-11 transcription (right). Plotted values represent the average ± SEM (right) 24 h post-infection.

(H) Phosphorylation of SIK2 at PKA target residues in response to Sendai virus infection. HFFF-TERT cells overexpressing SIK2-HA-FLAG were infected with Sendai virus ± 20 μM diclofenac for 24 h prior to lysis and immunoprecipitation with anti-HA antibody conjugated agarose beads. Input and immunoprecipitation eluate were analyzed by immunoblot for pPKA substrate and HA. $n = 3$, quantitation is to the right. Error bars: SEM.

(I and J) Depletion of MAVS prevents induction of COX2 in response to Sendai virus infection and prevents nuclear translocation of CRTC2 and CRTC3. (I) Immunoblot for COX2 and MAVS in the presence or absence of siRNA for MAVS or control. (J) Quantification of nuclear:cytoplasmic intensity of stably expressed CRTC2 or CRTC3 72 h after depletion of MAVS or control using siRNA, followed by 8 h Sendai infection. Representative immunofluorescence images are shown in Figure S6E. $^{*}p < 0.05$, $^{**}p < 0.01$, and $^{****}p < 0.0001$.

this route. This has been observed in response to RNA polymerase III (RNA PolIII)-transcribed exogenous DNAs, DNA virus-encoded RNA transcripts, and DNA virus-induced transcription of immunostimulatory host RNAs (reviewed in Zhao and Karijolich[53]). The role of IL-11 in infection remains unclear, but we hypothesized that IL-11 might prime cells for defense against viral infection. We therefore stimulated HFFF-TERT cells with IL-11 and IL-11RA (i.e., *trans*-signaling[54]) and profiled their transcriptional responses (Figures S8A–S8C; Table S5). DAVID functional enrichment analysis of transcripts significantly upregulated more than 2-fold following stimulation also identified a number of terms relating to the cell membrane, the pathogen recognition receptor (PRR) signaling pathway, and metabolism (Figure S8D; Table S6). The link to metabolism is of particular interest given that IL-11 has recently been linked to metabolism and aging *in vivo*.[55] Upregulated transcripts associated with pattern recognition included CASP1, NOD1, AIM2, and CGAS, suggesting that IL-11 may play a role preparing cells to defend against infection.

Transcriptional upregulation of IL-11 in PBMCs from patients with severe COVID-19

Several viral infections are known to induce pulmonary fibrosis, including SARS-CoV-2, influenza, and HCMV.[56–58] Pulmonary fibrosis frequently complicates COVID-19, although the pathogenesis is unclear. 2%–6% of patients with moderate COVID-19 develop fibrosis,[59] rising to 20%–72% if supplemental oxygen or ventilatory support is required.[60] Since these changes can be irreversible, new predictive tests and treatments are urgently required.

IL-11 is increased in many fibrotic diseases,[61–63] and blocking IL-11 with neutralizing monoclonal antibodies can prevent end-organ damage.[64] However, to our knowledge, there is little available information on a possible role for IL-11 driving COVID-19-associated pulmonary fibrosis, which might be secreted secondary to nuclear translocation of CRTC2/3 after viral sensing. One important study compared peripheral blood mononuclear cell (PBMC) transcriptional profiles from individuals with severe COVID-19 requiring intensive care to those of patients in intensive care without SARS-CoV-2[65] and people with mild COVID-19. We were, therefore, able to test the hypothesis that IL-11 is raised in severe COVID-19. Interestingly, IL-11 transcripts were significantly higher in PBMCs from patients with severe COVID-19 compared to non-SARS-CoV-2 intensive care controls (Figure S9). IL-11 transcripts were similarly higher, albeit without significance in PBMCs from patients with mild COVID-19 compared to uninfected controls.

DISCUSSION

The detection of pathogens and danger signals through cellular sensors is a defining principle of innate immunity. Although certain core components of the cellular response to viral infection have been extensively studied, systematic unbiased studies of protein translocation offer the potential to identify previously unappreciated signaling components.[14,66,67] Here, we identify CRTC2 and CRTC3 as components of the response to viral infection in a pathway downstream of MAVS that is reliant on the production of PGE2 and highlight IL-11 as a secreted cytokine dependent on these coactivators.

The CREB-regulated transcriptional coactivators (also known as the TORC proteins) are a family of structurally related CREB-binding proteins that are held inactive in the cytosol by a phosphorylation-dependent interaction with 14-3-3-family proteins (Figure 3A). Upon stimulation, they are dephosphorylated and translocate to the nucleus, where they enhance the transcriptional action of CREB in a manner independent of the phosphorylation state of CREB.[30,31,68] Our data demonstrate that transcriptional targets are shared between CRTC2 and CRTC3. This is consistent with previous structural studies of CRTC2 that showed that although CRTC2 makes some contact with DNA, this is for recognition of the minor grove rather than sequence-specific base binding.[69] The fact that CRTC2 has this groove specificity may explain the differential dependence of promoters on CREB and the CRTCs. Similar structural studies of CRTC3 in complex with DNA have not yet been performed. The human genome encodes CRTC1, -2, and -3, although expression varies by tissue type. For example, CRTC1 was poorly expressed in HFFF-TERT cells, whereas cells in the central nervous system are reported to express high levels of CRTC1.[31,70] Although all three bind to CREB via their N-terminal CREB binding domains, differentiation of function may occur at the level of activation. CRTC1 and CRTC2 have previously been characterized as being released from their 14-3-3 cytosolic partners following the action of the phosphatase calcineurin, whereas CRTC3 relies on dephosphorylation by PP2A following a distinct phosphorylation event by MAP kinases or cyclin-dependent kinases (CDKs).[32] This differential activation may explain the difference in translocation kinetics seen in this study, and potentially provide an evolutionary rationale for coactivators targeting the same subset of genes, but in response to distinct triggers. Given our observation of a role for CRTC2 and 3 in an inflammatory context it is interesting to note that CRTC3 and the adenylyl cyclase-linked PGE2 receptor EP4 have previously been linked to inflammatory bowel disease by genome wide association studies, as has IL-10, which is known to be a CRTC3 transcriptional target in certain cell types.[71,72]

IL-11 has hitherto been an under-characterized cytokine, with differing reports on its role in hematopoiesis.[73–76] IL-11 signals via the IL-11 receptor in complex with the protein gp130, which it shares with receptors for IL-6, IL-27, oncostatin M (OSM), leukemia inhibitory factor (LIF), ciliary neurotrophic factor (CNF), cardiotrophin-1 (CT-1), and cardiotrophin-like cytokine factor 1 (CLCF1). Signaling via IL-11 has recently been implicated in the release of inflammatory cytokines such as tumor necrosis factor alpha (TNF-α), CCL2, and CCL5 in the context of diet-induced steatohepatitis, cardiac fibrosis, and experimentally induced lung fibrosis.[61–63] Although IL-11 release has been previously observed to be released in the context of viral infection,[37–39] or induced by IL-1B,[77] its role at the organism level in the context of viral infection requires further research. Our transcriptomic analysis of IL-11 + IL-11RA suggests a possible role for IL-11 in paracrine signaling to ready defenses in cells neighboring those that are infected. This is supported by prior transcriptional studies finding that IL-11 treatment can induce pro-inflammatory cytokine release.[78]

Here, we identify CRTC2 and CRTC3 as components of the response to viral infection, characterize components required for their nuclear import, and identify a subset of genes upregulated in viral infection in a CRTC-dependent manner. We observe a role for prostaglandins in the movement of both CRTC2 and CRTC3 into the nucleus, and as such, it will be interesting to assess the impact of commonly used non-steroidal anti-inflammatories, such as ibuprofen, on circulating IL-11. This study highlights how spatial proteomics enables the systematic mapping of immunologically relevant signaling pathways.

Limitations of this study

Although this work sheds light on a signaling pathway previously unappreciated in viral infection, we acknowledge the limitations of this study. Primarily, our work was *in vitro*, and although our findings fit with an evolving model from the published literature, *in vivo* studies will be required to confirm a role for the CRTCs and IL-11 in viral pathology. It is intriguing to note that IL-11 transcripts were higher in PBMCs from SARS-CoV-2 patients in intensive care units than non-SARS-CoV-2-infected intensive care controls, particularly as SARS-CoV-2 infection has been associated with lung fibrosis in over 70% of those requiring mechanical ventilation.[60] This may indicate a role for CRTC-mediated viral signaling in the pathogenesis of this important disease. Further research in this area is clearly warranted, particularly given the existence of IL-11-neutralizing monoclonal antibodies, which have been shown to reverse IL-11-induced organ damage and fibrosis in other experimental pathological settings.[61,79,80] Additionally, although we focus on the cAMP-mediated activation of CRTC2 and CRTC3 in viral infection, further work is required to determine whether other signaling pathways reported to stimulate CRTC movement play a role in viral infection.[32]

RESOURCE AVAILABILITY

Lead contact

Further information and requests for resources and reagents should be directed to and will be fulfilled by the lead contact, Michael P. Weekes (mpw1001@cam.ac.uk).

Materials availability

Materials generated in this study are available upon request to the corresponding author.

Data and code availability

- Data: unprocessed peptide data for Figures 1 and S1 are available at https://doi.org/10.17632/8phtpvbvgs.1. This file includes details of peptide sequences, redundancy, protein assignment, raw unprocessed TMT reporter intensities, and isolation specificity. The mass spectrometry proteomics data have been deposited to the ProteomeXchange Consortium via the PRIDE[81] partner repository with the dataset identifier PXD051850. The RNA-seq raw data files generated in this study are available via the ArrayExpress database with accession E-MTAB-14001 and E-MTAB-14684. All raw data and any information required to reanalyze the data in this manuscript are available upon request.
- Code: no new code was generated in this study.

ACKNOWLEDGMENTS

We are grateful to Prof. Steven Gygi for providing access to the "MassPike" software pipeline for quantitative proteomics. We are also grateful to the Cambridge Institute for Medical Research core facilities in flow cytometry and microscopy. This work was supported by a Medical Research Council project grant (MR/W025647/1) to M.P.W., an Addenbrooke's Charitable Trust grant (900408) to M.P.W., an Evelyn Trust fellowship (project reference 18/27) to B.J.R., an Evelyn Trust grant (20/75) to P.A.L., a Medical Research Council fellowship and BBSRC project grants to B.C. (MR/R021821/1, BB/X001261/1, BB/V017780/1, and BB/V006096/1), and the NIHR Cambridge Biomedical Research Centre (NIHR203312). G.H.H.B. was supported by the Max Planck Society for the Advancement of Science. The views expressed are those of the authors and not necessarily those of the NIHR or the Department of Health and Social Care. For the purpose of open access, the authors have applied a CC-BY public copyright license to any author-accepted manuscript version arising from this submission.

AUTHOR CONTRIBUTIONS

Conceptualization, M.P.W.; investigation, B.J.R., M.O., G.W., Y.D., C.T.R.D., Y.L., R.A., G.E., N.I., D.J.H., P.A.L., B.C., and G.H.H.B.; data analysis, B.J.R., M.O., G.W., and M.P.W.; funding acquisition, B.J.R., B.C., and M.P.W.; supervision, B.C., G.H.H.B., and M.P.W.; writing, B.J.R., M.O., G.W., and M.P.W. All authors edited the manuscript.

DECLARATION OF INTERESTS

The authors declare no competing interests.

STAR★METHODS

Detailed methods are provided in the online version of this paper and include the following:

- KEY RESOURCES TABLE
- EXPERIMENTAL MODEL AND SUBJECT DETAILS
  - Cells and cell culture
  - Viruses and cellular stimuli
- METHOD DETAILS
  - Plasmid construction
  - Stable cell lines
  - Immunoblotting
  - Immunofluorescence
  - RNA extraction, cDNA and qPCR
  - Synthego Cas9/CRISPR
  - Drugs & Ligands
  - Immunoprecipitation
  - siRNAs
  - ELISA
  - RNAseq
  - Subcellular fractionation
  - Whole cell lysate protein digestion for proteomics
  - Peptide labeling with tandem mass tags (TMT)
  - Offline HpRP fractionation
  - LC-MS3
- QUANTIFICATION AND STATISTICAL ANALYSIS
  - Proteomic data analysis
  - Pathway analysis
  - Cellprofiler
  - Sequence alignment
  - Statistical analysis of qPCR and ELISA data

SUPPLEMENTAL INFORMATION

Supplemental information can be found online at https://doi.org/10.1016/j.celrep.2025.115263.

Received: May 2, 2024
Revised: December 9, 2024
Accepted: January 12, 2025

REFERENCES

1. Horner, S.M., Liu, H.M., Park, H.S., Briley, J., and Gale, M., Jr. (2011). Mitochondrial-associated endoplasmic reticulum membranes (MAM) form innate immune synapses and are targeted by hepatitis C virus. Proc. Natl. Acad. Sci. USA *108*, 14590–14595. https://doi.org/10.1073/pnas.1110133108.
2. Saitoh, T., Fujita, N., Hayashi, T., Takahara, K., Satoh, T., Lee, H., Matsunaga, K., Kageyama, S., Omori, H., Noda, T., et al. (2009). Atg9a controls dsDNA-driven dynamic translocation of STING and the innate immune response. Proc. Natl. Acad. Sci. USA *106*, 20842–20846. https://doi.org/10.1073/pnas.0911267106.
3. Mukai, K., Konno, H., Akiba, T., Uemura, T., Waguri, S., Kobayashi, T., Barber, G.N., Arai, H., and Taguchi, T. (2016). Activation of STING requires palmitoylation at the Golgi. Nat. Commun. *7*, 11932. https://doi.org/10.1038/ncomms11932.
4. Seth, R.B., Sun, L., Ea, C.K., and Chen, Z.J. (2005). Identification and characterization of MAVS, a mitochondrial antiviral signaling protein that activates NF-kappaB and IRF 3. Cell *122*, 669–682. https://doi.org/10.1016/j.cell.2005.08.012.
5. Abe, T., and Barber, G.N. (2014). Cytosolic-DNA-mediated, STING-dependent proinflammatory gene induction necessitates canonical NF-kappaB activation through TBK1. J. Virol. *88*, 5328–5341. https://doi.org/10.1128/JVI.00037-14.
6. Ishikawa, H., and Barber, G.N. (2008). STING is an endoplasmic reticulum adaptor that facilitates innate immune signalling. Nature *455*, 674–678. https://doi.org/10.1038/nature07317.
7. Liu, T., Zhang, L., Joo, D., and Sun, S.C. (2017). NF-kappaB signaling in inflammation. Signal Transduct. Targeted Ther. *2*, 17023. https://doi.org/10.1038/sigtrans.2017.23.
8. Al Hamrashdi, M., and Brady, G. (2022). Regulation of IRF3 activation in human antiviral signaling pathways. Biochem. Pharmacol. *200*, 115026. https://doi.org/10.1016/j.bcp.2022.115026.
9. Wang, J., Li, P., and Wu, M.X. (2016). Natural STING Agonist as an "Ideal" Adjuvant for Cutaneous Vaccination. J. Invest. Dermatol. *136*, 2183–2191. https://doi.org/10.1016/j.jid.2016.05.105.
10. Wang, J., Li, P., Yu, Y., Fu, Y., Jiang, H., Lu, M., Sun, Z., Jiang, S., Lu, L., and Wu, M.X. (2020). Pulmonary surfactant-biomimetic nanoparticles potentiate heterosubtypic influenza immunity. Science *367*, eaau0810. https://doi.org/10.1126/science.aau0810.
11. Motwani, M., Pesiridis, S., and Fitzgerald, K.A. (2019). DNA sensing by the cGAS-STING pathway in health and disease. Nat. Rev. Genet. *20*, 657–674. https://doi.org/10.1038/s41576-019-0151-1.
12. Jiao, S., Guan, J., Chen, M., Wang, W., Li, C., Wang, Y., Cheng, Y., and Zhou, Z. (2018). Targeting IRF3 as a YAP agonist therapy against gastric cancer. J. Exp. Med. *215*, 699–718. https://doi.org/10.1084/jem.20171116.
13. Itzhak, D.N., Davies, C., Tyanova, S., Mishra, A., Williamson, J., Antrobus, R., Cox, J., Weekes, M.P., and Borner, G.H.H. (2017). A mass spectrometry-based approach for mapping protein subcellular localization reveals the spatial proteome of mouse primary neurons. Cell Rep. *20*, 2706–2718.
14. Itzhak, D.N., Tyanova, S., Cox, J., and Borner, G.H. (2016). Global, quantitative and dynamic mapping of protein subcellular localization. Elife *5*, e16950. https://doi.org/10.7554/eLife.16950.
15. Schessner, J.P., Albrecht, V., Davies, A.K., Sinitcyn, P., and Borner, G.H.H. (2023). Deep and fast label-free Dynamic Organellar Mapping. Nat. Commun. *14*, 5252. https://doi.org/10.1038/s41467-023-41000-7.
16. Martinez-Gil, L., Goff, P.H., Hai, R., Garcia-Sastre, A., Shaw, M.L., and Palese, P. (2013). A Sendai virus-derived RNA agonist of RIG-I as a virus vaccine adjuvant. J. Virol. *87*, 1290–1300. https://doi.org/10.1128/JVI.02338-12.
17. Baum, A., Sachidanandam, R., and García-Sastre, A. (2010). Preference of RIG-I for short viral RNA molecules in infected cells revealed by next-generation sequencing. Proc. Natl. Acad. Sci. USA *107*, 16303–16308. https://doi.org/10.1073/pnas.1005077107.
18. Nightingale, K., Lin, K.M., Ravenhill, B.J., Davies, C., Nobre, L., Fielding, C.A., Ruckova, E., Fletcher-Etherington, A., Soday, L., Nichols, H., et al. (2018). High-definition analysis of host protein stability during Human Cytomegalovirus infection reveals antiviral factors and viral evasion mechanisms. Cell Host Microbe *24*, 447–460. https://doi.org/10.1016/j.chom.2018.07.011.
19. Cox, J., and Mann, M. (2008). MaxQuant enables high peptide identification rates, individualized ppb-range mass accuracies and proteome-wide protein quantification. Nat. Biotechnol. *26*, 1367–1372. https://doi.org/10.1038/nbt.1511.
20. Kwon, J.W., Kwon, H.K., Shin, H.J., Choi, Y.M., Anwar, M.A., and Choi, S. (2015). Activating transcription factor 3 represses inflammatory responses by binding to the p65 subunit of NF-κB. Sci. Rep. *5*, 14470. https://doi.org/10.1038/srep14470.
21. Liu, S., Li, Z., Lan, S., Hao, H., Baz, A.A., Yan, X., Gao, P., Chen, S., and Chu, Y. (2024). The Dual Roles of Activating Transcription Factor 3 (ATF3) in Inflammation, Apoptosis, Ferroptosis, and Pathogen Infection Responses. Int. J. Mol. Sci. *25*, 824. https://doi.org/10.3390/ijms25020824.
22. Lu, Y., Stuart, J.H., Talbot-Cooper, C., Agrawal-Singh, S., Huntly, B., Smid, A.I., Snowden, J.S., Dupont, L., and Smith, G.L. (2019). Histone deacetylase 4 promotes type I interferon signaling, restricts DNA viruses, and is degraded via vaccinia virus protein C6. Proc. Natl. Acad. Sci. USA *116*, 11997–12006. https://doi.org/10.1073/pnas.1816399116.
23. Soday, L., Lu, Y., Albarnaz, J.D., Davies, C.T.R., Antrobus, R., Smith, G.L., and Weekes, M.P. (2019). Quantitative temporal proteomic analysis of vaccinia virus infection reveals regulation of histone deacetylases by an interferon antagonist. Cell Rep. *27*, 1920–1933.e7.
24. Gulyás, G., Sohn, M., Kim, Y.J., Várnai, P., and Balla, T. (2020). ORP3 phosphorylation regulates phosphatidylinositol 4-phosphate and Ca(2+) dynamics at plasma membrane-ER contact sites. J. Cell Sci. *133*, jcs237388. https://doi.org/10.1242/jcs.237388.
25. Ivashkiv, L.B., and Donlin, L.T. (2014). Regulation of type I interferon responses. Nat. Rev. Immunol. *14*, 36–49. https://doi.org/10.1038/nri3581.
26. Rusinova, I., Forster, S., Yu, S., Kannan, A., Masse, M., Cumming, H., Chapman, R., and Hertzog, P.J. (2013). Interferome v2.0: an updated database of annotated interferon-regulated genes. Nucleic Acids Res. *41*, D1040–D1046. https://doi.org/10.1093/nar/gks1215.
27. Ramirez, R.D., Sheridan, S., Girard, L., Sato, M., Kim, Y., Pollack, J., Peyton, M., Zou, Y., Kurie, J.M., Dimaio, J.M., et al. (2004). Immortalization of human bronchial epithelial cells in the absence of viral oncoproteins. Cancer Res. *64*, 9027–9034. https://doi.org/10.1158/0008-5472.CAN-04-3703.
28. Iourgenko, V., Zhang, W., Mickanin, C., Daly, I., Jiang, C., Hexham, J.M., Orth, A.P., Miraglia, L., Meltzer, J., Garza, D., et al. (2003). Identification of a family of cAMP response element-binding protein coactivators by genome-scale functional analysis in mammalian cells. Proc. Natl. Acad. Sci. USA *100*, 12147–12152. https://doi.org/10.1073/pnas.1932773100.
29. Tasoulas, J., Rodon, L., Kaye, F.J., Montminy, M., and Amelio, A.L. (2019). Adaptive Transcriptional Responses by CRTC Coactivators in Cancer. Trends Cancer *5*, 111–127. https://doi.org/10.1016/j.trecan.2018.12.002.
30. Conkright, M.D., Canettieri, G., Screaton, R., Guzman, E., Miraglia, L., Hogenesch, J.B., and Montminy, M. (2003). TORCs: transducers of regulated CREB activity. Mol. Cell *12*, 413–423. https://doi.org/10.1016/j.molcel.2003.08.013.
31. Sonntag, T., Moresco, J.J., Vaughan, J.M., Matsumura, S., Yates, J.R., 3rd, and Montminy, M. (2017). Analysis of a cAMP regulated coactivator family reveals an alternative phosphorylation motif for AMPK family members. PLoS One *12*, e0173013. https://doi.org/10.1371/journal.pone.0173013.

32. Sonntag, T., Ostojić, J., Vaughan, J.M., Moresco, J.J., Yoon, Y.S., Yates, J.R., 3rd, and Montminy, M. (2019). Mitogenic signals stimulate the CREB coactivator CRTC3 through PP2A recruitment. iScience *11*, 134–145. https://doi.org/10.1016/j.isci.2018.12.012.

33. Ng, B., Cook, S.A., and Schafer, S. (2020). Interleukin-11 signaling underlies fibrosis, parenchymal dysfunction, and chronic inflammation of the airway. Exp. Mol. Med. *52*, 1871–1878. https://doi.org/10.1038/s12276-020-00531-5.

34. Fung, K.Y., Louis, C., Metcalfe, R.D., Kosasih, C.C., Wicks, I.P., Griffin, M.D.W., and Putoczki, T.L. (2022). Emerging roles for IL-11 in inflammatory diseases. Cytokine *149*, 155750. https://doi.org/10.1016/j.cyto.2021.155750.

35. Seyedsadr, M., Wang, Y., Elzoheiry, M., Shree Gopal, S., Jang, S., Duran, G., Chervoneva, I., Kasimoglou, E., Wrobel, J.A., Hwang, D., et al. (2023). IL-11 induces NLRP3 inflammasome activation in monocytes and inflammatory cell migration to the central nervous system. Proc. Natl. Acad. Sci. USA *120*, e2221007120. https://doi.org/10.1073/pnas.2221007120.

36. Schafer, S., Viswanathan, S., Widjaja, A.A., Lim, W.W., Moreno-Moral, A., DeLaughter, D.M., Ng, B., Patone, G., Chow, K., Khin, E., et al. (2017). IL-11 is a crucial determinant of cardiovascular fibrosis. Nature *552*, 110–115. https://doi.org/10.1038/nature24676.

37. Einarsson, O., Geba, G.P., Zhu, Z., Landry, M., and Elias, J.A. (1996). Interleukin-11: stimulation in vivo and in vitro by respiratory viruses and induction of airways hyperresponsiveness. J. Clin. Invest. *97*, 915–924. https://doi.org/10.1172/JCI118514.

38. Bartz, H., Büning-Pfaue, F., Türkel, O., and Schauer, U. (2002). Respiratory syncytial virus induces prostaglandin E2, IL-10 and IL-11 generation in antigen presenting cells. Clin. Exp. Immunol. *129*, 438–445. https://doi.org/10.1046/j.1365-2249.2002.01927.x.

39. Gustafsson, K.L.R., Renné, T., Söderberg-Naucler, C., and Butler, L.M. (2018). Human cytomegalovirus replication induces endothelial cell interleukin-11. Cytokine *111*, 563–566. https://doi.org/10.1016/j.cyto.2018.05.018.

40. Kim, J.H., Hedrick, S., Tsai, W.W., Wiater, E., Le Lay, J., Kaestner, K.H., Leblanc, M., Loar, A., and Montminy, M. (2017). CREB coactivators CRTC2 and CRTC3 modulate bone marrow hematopoiesis. Proc. Natl. Acad. Sci. USA *114*, 11739–11744. https://doi.org/10.1073/pnas.1712616114.

41. Ye, F., Alvarez-Carbonell, D., Nguyen, K., Leskov, K., Garcia-Mesa, Y., Sreeram, S., Valadkhan, S., and Karn, J. (2022). Recruitment of the CoREST transcription repressor complexes by Nerve Growth factor IB-like receptor (Nurr1/NR4A2) mediates silencing of HIV in microglial cells. PLoS Pathog. *18*, e1010110. https://doi.org/10.1371/journal.ppat.1010110.

42. Kozhemyakina, E., Cohen, T., Yao, T.P., and Lassar, A.B. (2009). Parathyroid hormone-related peptide represses chondrocyte hypertrophy through a protein phosphatase 2A/histone deacetylase 4/MEF2 pathway. Mol. Cell Biol. *29*, 5751–5762. https://doi.org/10.1128/MCB.00415-09.

43. Belfield, J.L., Whittaker, C., Cader, M.Z., and Chawla, S. (2006). Differential effects of Ca2+ and cAMP on transcription mediated by MEF2D and cAMP-response element-binding protein in hippocampal neurons. J. Biol. Chem. *281*, 27724–27732. https://doi.org/10.1074/jbc.M601485200.

44. Sonntag, T., Vaughan, J.M., and Montminy, M. (2018). 14-3-3 proteins mediate inhibitory effects of cAMP on salt-inducible kinases (SIKs). FEBS J. *285*, 467–480. https://doi.org/10.1111/febs.14351.

45. Henriksson, E., Säll, J., Gormand, A., Wasserstrom, S., Morrice, N.A., Fritzen, A.M., Foretz, M., Campbell, D.G., Sakamoto, K., Ekelund, M., et al. (2015). SIK2 regulates CRTCs, HDAC4 and glucose uptake in adipocytes. J. Cell Sci. *128*, 472–486. https://doi.org/10.1242/jcs.153932.

46. Kirkby, N.S., Zaiss, A.K., Wright, W.R., Jiao, J., Chan, M.V., Warner, T.D., Herschman, H.R., and Mitchell, J.A. (2013). Differential COX-2 induction by viral and bacterial PAMPs: Consequences for cytokine and interferon responses and implications for anti-viral COX-2 directed therapies. Biochem. Biophys. Res. Commun. *438*, 249–256. https://doi.org/10.1016/j.bbrc.2013.07.006.

47. Rumzhum, N.N., and Ammit, A.J. (2016). Cyclooxygenase 2: its regulation, role and impact in airway inflammation. Clin. Exp. Allergy *46*, 397–410. https://doi.org/10.1111/cea.12697.

48. Blomqvist, A., and Engblom, D. (2018). Neural Mechanisms of Inflammation-Induced Fever. Neuroscientist *24*, 381–399. https://doi.org/10.1177/1073858418760481.

49. Ricciotti, E., and FitzGerald, G.A. (2011). Prostaglandins and inflammation. Arterioscler. Thromb. Vasc. Biol. *31*, 986–1000. https://doi.org/10.1161/ATVBAHA.110.207449.

50. MacKenzie, K.F., Clark, K., Naqvi, S., McGuire, V.A., Nöehren, G., Kristariyanto, Y., van den Bosch, M., Mudaliar, M., McCarthy, P.C., Pattison, M.J., et al. (2013). PGE(2) induces macrophage IL-10 production and a regulatory-like phenotype via a protein kinase A-SIK-CRTC3 pathway. J. Immunol. *190*, 565–577. https://doi.org/10.4049/jimmunol.1202462.

51. Sugimoto, Y., and Narumiya, S. (2007). Prostaglandin E receptors. J. Biol. Chem. *282*, 11613–11617. https://doi.org/10.1074/jbc.R600038200.

52. Kaltschmidt, B., Linker, R.A., Deng, J., and Kaltschmidt, C. (2002). Cyclooxygenase-2 is a neuronal target gene of NF-kappaB. BMC Mol. Biol. *3*, 16. https://doi.org/10.1186/1471-2199-3-16.

53. Zhao, Y., and Karijolich, J. (2019). Know Thyself: RIG-I-Like Receptor Sensing of DNA Virus Infection. J. Virol. *93*, e01085-19. https://doi.org/10.1128/jvi.01085-19.

54. Lokau, J., Nitz, R., Agthe, M., Monhasery, N., Aparicio-Siegmund, S., Schumacher, N., Wolf, J., Möller-Hackbarth, K., Waetzig, G.H., Grötzinger, J., et al. (2016). Proteolytic Cleavage Governs Interleukin-11 Trans-signaling. Cell Rep. *14*, 1761–1773. https://doi.org/10.1016/j.celrep.2016.01.053.

55. Widjaja, A.A., Lim, W.W., Viswanathan, S., Chothani, S., Corden, B., Dasan, C.M., Goh, J.W.T., Lim, R., Singh, B.K., Tan, J., et al. (2024). Inhibition of IL-11 signalling extends mammalian healthspan and lifespan. Nature *632*, 157–165. https://doi.org/10.1038/s41586-024-07701-9.

56. Ojha, V., Mani, A., Pandey, N.N., Sharma, S., and Kumar, S. (2020). CT in coronavirus disease 2019 (COVID-19): a systematic review of chest CT findings in 4410 adult patients. Eur. Radiol. *30*, 6129–6138. https://doi.org/10.1007/s00330-020-06975-7.

57. Nakajima, N., Sato, Y., Katano, H., Hasegawa, H., Kumasaka, T., Hata, S., Tanaka, S., Amano, T., Kasai, T., Chong, J.M., et al. (2012). Histopathological and immunohistochemical findings of 20 autopsy cases with 2009 H1N1 virus infection. Mod. Pathol. *25*, 1–13. https://doi.org/10.1038/modpathol.2011.125.

58. Coclite, E., Di Natale, C., and Nigro, G. (2013). Congenital and perinatal cytomegalovirus lung infection. J. Matern. Fetal Neonatal Med. *26*, 1671–1675. https://doi.org/10.3109/14767058.2013.794207.

59. Bazdyrev, E., Rusina, P., Panova, M., Novikov, F., Grishagin, I., and Nebolsin, V. (2021). Lung Fibrosis after COVID-19: Treatment Prospects. Pharmaceuticals *14*, 807. https://doi.org/10.3390/ph14080807.

60. McGroder, C.F., Zhang, D., Choudhury, M.A., Salvatore, M.M., D'Souza, B.M., Hoffman, E.A., Wei, Y., Baldwin, M.R., and Garcia, C.K. (2021). Pulmonary fibrosis 4 months after COVID-19 is associated with severity of illness and blood leucocyte telomere length. Thorax *76*, 1242–1245. https://doi.org/10.1136/thoraxjnl-2021-217031.

61. Widjaja, A.A., Singh, B.K., Adami, E., Viswanathan, S., Dong, J., D'Agostino, G.A., Ng, B., Lim, W.W., Tan, J., Paleja, B.S., et al. (2019). Inhibiting Interleukin 11 Signaling Reduces Hepatocyte Death and Liver Fibrosis, Inflammation, and Steatosis in Mouse Models of Nonalcoholic Steatohepatitis. Gastroenterology *157*, 777–792.e14. https://doi.org/10.1053/j.gastro.2019.05.002.

62. Sweeney, M., O'Fee, K., Villanueva-Hayes, C., Rahman, E., Lee, M., Vanezis, K., Andrew, I., Lim, W.W., Widjaja, A., Barton, P.J.R., and Cook,

S.A. (2023). Cardiomyocyte-Restricted Expression of IL11 Causes Cardiac Fibrosis, Inflammation, and Dysfunction. Int. J. Mol. Sci. *24*, 1–14. https://doi.org/10.3390/ijms241612989.

63. Ng, B., Dong, J., Viswanathan, S., Widjaja, A.A., Paleja, B.S., Adami, E., Ko, N.S.J., Wang, M., Lim, S., Tan, J., et al. (2020). Fibroblast-specific IL11 signaling drives chronic inflammation in murine fibrotic lung disease. FASEB J *34*, 11802–11815. https://doi.org/10.1096/fj.202001045RR.

64. Cook, S.A., and Schafer, S. (2020). Hiding in Plain Sight: Interleukin-11 Emerges as a Master Regulator of Fibrosis, Tissue Integrity, and Stromal Inflammation. Annu. Rev. Med. *71*, 263–276. https://doi.org/10.1146/annurev-med-041818-011649.

65. Shaath, H., and Alajez, N.M. (2021). Identification of PBMC-based molecular signature associational with COVID-19 disease severity. Heliyon *7*, e06866. https://doi.org/10.1016/j.heliyon.2021.e06866.

66. Davies, A.K., Alecu, J.E., Ziegler, M., Vasilopoulou, C.G., Merciai, F., Jumo, H., Afshar-Saber, W., Sahin, M., Ebrahimi-Fakhari, D., and Borner, G.H.H. (2022). AP-4-mediated axonal transport controls endocannabinoid production in neurons. Nat. Commun. *13*, 1058. https://doi.org/10.1038/s41467-022-28609-w.

67. Krahmer, N., Najafi, B., Schueder, F., Quagliarini, F., Steger, M., Seitz, S., Kasper, R., Salinas, F., Cox, J., Uhlenhaut, N.H., et al. (2018). Organellar Proteomics and Phospho-Proteomics Reveal Subcellular Reorganization in Diet-Induced Hepatic Steatosis. Dev. Cell *47*, 205–221.e7. https://doi.org/10.1016/j.devcel.2018.09.017.

68. Screaton, R.A., Conkright, M.D., Katoh, Y., Best, J.L., Canettieri, G., Jeffries, S., Guzman, E., Niessen, S., Yates, J.R., 3rd, Takemori, H., et al. (2004). The CREB coactivator TORC2 functions as a calcium- and cAMP-sensitive coincidence detector. Cell *119*, 61–74. https://doi.org/10.1016/j.cell.2004.09.015.

69. Song, Y., Zhai, L., Valencia Swain, J., Chen, Y., Wang, P., Chen, L., Liu, Y., and Xiang, S. (2018). Structural Insights into the CRTC2-CREB Complex Assembly on CRE. J. Mol. Biol. *430*, 1926–1939. https://doi.org/10.1016/j.jmb.2018.04.038.

70. Altarejos, J.Y., and Montminy, M. (2011). CREB and the CRTC co-activators: sensors for hormonal and metabolic signals. Nat. Rev. Mol. Cell Biol. *12*, 141–151. https://doi.org/10.1038/nrm3072.

71. Jostins, L., Ripke, S., Weersma, R.K., Duerr, R.H., McGovern, D.P., Hui, K.Y., Lee, J.C., Schumm, L.P., Sharma, Y., Anderson, C.A., et al. (2012). Host-microbe interactions have shaped the genetic architecture of inflammatory bowel disease. Nature *491*, 119–124. https://doi.org/10.1038/nature11582.

72. Wein, M.N., Foretz, M., Fisher, D.E., Xavier, R.J., and Kronenberg, H.M. (2018). Salt-Inducible Kinases: Physiology, Regulation by cAMP, and Therapeutic Potential. Trends Endocrinol. Metab. *29*, 723–735. https://doi.org/10.1016/j.tem.2018.08.004.

73. Paul, S.R., Bennett, F., Calvetti, J.A., Kelleher, K., Wood, C.R., O'Hara, R.M., Jr., Leary, A.C., Sibley, B., Clark, S.C., Williams, D.A., et al. (1990). Molecular cloning of a cDNA encoding interleukin 11, a stromal cell-derived lymphopoietic and hematopoietic cytokine. Proc. Natl. Acad. Sci. USA *87*, 7512–7516. https://doi.org/10.1073/pnas.87.19.7512.

74. Du, X.X., Neben, T., Goldman, S., and Williams, D.A. (1993). Effects of recombinant human interleukin-11 on hematopoietic reconstitution in transplant mice: acceleration of recovery of peripheral blood neutrophils and platelets. Blood *81*, 27–34.

75. Nandurkar, H.H., Robb, L., Tarlinton, D., Barnett, L., Köntgen, F., and Begley, C.G. (1997). Adult mice with targeted mutation of the interleukin-11 receptor (IL11Ra) display normal hematopoiesis. Blood *90*, 2148–2159.

76. Cook, S.A. (2023). Understanding interleukin 11 as a disease gene and therapeutic target. Biochem. J. *480*, 1987–2008. https://doi.org/10.1042/BCJ20220160.

77. Compton, S.E., Kitchen-Goosen, S.M., DeCamp, L.M., Lau, K.H., Mabvakure, B., Vos, M., Williams, K.S., Wong, K.K., Shi, X., Rothbart, S.B., et al. (2023). LKB1 controls inflammatory potential through CRTC2-dependent histone acetylation. Mol. Cell *83*, 1872–1886.e5. https://doi.org/10.1016/j.molcel.2023.04.017.

78. Widjaja, A.A., Chothani, S., Viswanathan, S., Goh, J.W.T., Lim, W.W., and Cook, S.A. (2022). IL11 Stimulates IL33 Expression and Proinflammatory Fibroblast Activation across Tissues. Int. J. Mol. Sci. *23*, 8900. https://doi.org/10.3390/ijms23168900.

79. Widjaja, A.A., Shekeran, S.G., Adami, E., Ting, J.G.W., Tan, J., Viswanathan, S., Lim, S.Y., Tan, P.H., Hübner, N., Coffman, T., and Cook, S.A. (2022). A Neutralizing IL-11 Antibody Improves Renal Function and Increases Lifespan in a Mouse Model of Alport Syndrome. J. Am. Soc. Nephrol. *33*, 718–730. https://doi.org/10.1681/ASN.2021040577.

80. Schumacher, D., Liehn, E.A., Nilcham, P., Mayan, D.C., Rattanasopa, C., Anand, K., Crespo-Avilan, G.E., Hernandez-Resendiz, S., Singaraja, R.R., Cook, S.A., and Hausenloy, D.J. (2021). A neutralizing IL-11 antibody reduces vessel hyperplasia in a mouse carotid artery wire injury model. Sci. Rep. *11*, 20674. https://doi.org/10.1038/s41598-021-99880-y.

81. Vizcaino, J.A., Csordas, A., del-Toro, N., Dianes, J.A., Griss, J., Lavidas, I., Mayer, G., Perez-Riverol, Y., Reisinger, F., Ternent, T., et al. (2016). 2016 update of the PRIDE database and its related tools. Nucleic acids research *44*, D447–D456. https://doi.org/10.1093/nar/gkv1145.

82. Stanton, R.J., Baluchova, K., Dargan, D.J., Cunningham, C., Sheehy, O., Seirafian, S., McSharry, B.P., Neale, M.L., Davies, J.A., Tomasec, P., et al. (2010). Reconstruction of the complete human cytomegalovirus genome in a BAC reveals RL13 to be a potent inhibitor of replication. J. Clin. Invest. *120*, 3191–3208. https://doi.org/10.1172/JCI42955.

83. Blanchard, T.J., Alcami, A., Andrea, P., and Smith, G.L. (1998). Modified vaccinia virus Ankara undergoes limited replication in human cells and lacks several immunomodulatory proteins: implications for use as a human vaccine. J. Gen. Virol. *79*, 1159–1167. https://doi.org/10.1099/0022-1317-79-5-1159.

84. Nagel, C.H., Pohlmann, A., and Sodeik, B. (2014). Construction and characterization of bacterial artificial chromosomes (BACs) containing herpes simplex virus full-length genomes. Methods Mol. Biol. *1144*, 43–62.

85. Stanton, R.J., McSharry, B.P., Rickards, C.R., Wang, E.C.Y., Tomasec, P., and Wilkinson, G.W.G. (2007). Cytomegalovirus destruction of focal adhesions revealed in a high-throughput Western blot analysis of cellular protein expression. J. Virol. *81*, 7860–7872. https://doi.org/10.1128/JVI.02247-06.

86. Zhu, Y., Li, J., Bo, H., He, D., Xiao, M., Xiang, L., Gong, L., Hu, Y., Zhang, Y., Cheng, Y., and Deng, L. (2020). LINC00467 is up-regulated by TDG-mediated acetylation in non-small cell lung cancer and promotes tumor progression. Oncogene *39*, 6071–6084.

87. Nishina, T., Deguchi, Y., Miura, R., Yamazaki, S., Shinkai, Y., Kojima, Y., Okumura, K., Kumagai, Y., and Nakano, H. (2017). Critical contribution of nuclear factor erythroid 2-related factor 2 (NRF2) to electrophile-induced interleukin-11 production. J. Biol. Chem. *292*, 205–216.

88. Marentette, J.O., Anderson, C.C., Prutton, K.M., Jennings, E.Q., Rauniyar, A.K., Galligan, J.J., and Roede, J.R. (2021). Trisomy 21 impairs PGE2 production in dermal fibroblasts. Prostaglandins Other Lipid Mediat. *153*, 106524.

89. Yamamichi, K., Fukuda, T., Sanui, T., Toyoda, K., Tanaka, U., Nakao, Y., Yotsumoto, K., Yamato, H., Taketomi, T., Uchiumi, T., and Nishimura, F. (2017). Amelogenin induces M2 macrophage polarisation via PGE2/cAMP signalling pathway. Arch. Oral Biol. *83*, 241–251.

90. Menzies, S.A., Volkmar, N., van den Boomen, D.J., Timms, R.T., Dickson, A.S., Nathan, J.A., and Lehner, P.J. (2018). The sterol-responsive RNF145 E3 ubiquitin ligase mediates the degradation of HMG-CoA reductase together with gp78 and Hrd1. Elife *7*, e40009. https://doi.org/10.7554/eLife.40009.

91. Dolan, A., Cunningham, C., Hector, R.D., Hassan-Walker, A.F., Lee, L., Addison, C., Dargan, D.J., McGeoch, D.J., Gatherer, D., Emery, V.C., et al. (2004). Genetic content of wild-type human cytomegalovirus. J. Gen. Virol. *85*, 1301–1312.

92. Law, M., and Smith, G.L. (2001). Antibody neutralization of the extracellular enveloped form of vaccinia virus. Virology *280*, 132–142. https://doi.org/10.1006/viro.2000.0750.

93. Gierasch, W.W., Zimmerman, D.L., Ward, S.L., Vanheyningen, T.K., Romine, J.D., and Leib, D.A. (2006). Construction and characterization of bacterial artificial chromosomes containing HSV-1 strains 17 and KOS. J. Virol. Methods *135*, 197–206. https://doi.org/10.1016/j.jviromet.2006.03.014.

94. Bushnell, B. BBMap. https://sourceforge.net/projects/bbmap/.

95. Dobin, A., Davis, C.A., Schlesinger, F., Drenkow, J., Zaleski, C., Jha, S., Batut, P., Chaisson, M., and Gingeras, T.R. (2013). STAR: ultrafast universal RNA-seq aligner. Bioinformatics *29*, 15–21. https://doi.org/10.1093/bioinformatics/bts635.

96. Anders, S., Pyl, P.T., and Huber, W. (2015). HTSeq–a Python framework to work with high-throughput sequencing data. Bioinformatics *31*, 166–169. https://doi.org/10.1093/bioinformatics/btu638.

97. Robinson, M.D., McCarthy, D.J., and Smyth, G.K. (2010). edgeR: a Bioconductor package for differential expression analysis of digital gene expression data. Bioinformatics *26*, 139–140. https://doi.org/10.1093/bioinformatics/btp616.

98. McAlister, G.C., Nusinow, D.P., Jedrychowski, M.P., Wühr, M., Huttlin, E.L., Erickson, B.K., Rad, R., Haas, W., and Gygi, S.P. (2014). MultiNotch MS3 enables accurate, sensitive, and multiplexed detection of differential expression across cancer cell line proteomes. Anal. Chem. *86*, 7150–7158. https://doi.org/10.1021/ac502040v.

99. Haas, W., Faherty, B.K., Gerber, S.A., Elias, J.E., Beausoleil, S.A., Bakalarski, C.E., Li, X., Villén, J., and Gygi, S.P. (2006). Optimization and use of peptide mass measurement accuracy in shotgun proteomics. Mol. Cell. Proteomics *5*, 1326–1337. https://doi.org/10.1074/mcp.M500339-MCP200.

100. Elias, J.E., and Gygi, S.P. (2007). Target-decoy search strategy for increased confidence in large-scale protein identifications by mass spectrometry. Nat. Methods *4*, 207–214. https://doi.org/10.1038/nmeth1019.

101. Elias, J.E., and Gygi, S.P. (2010). Target-decoy search strategy for mass spectrometry-based proteomics. Methods Mol. Biol. *604*, 55–71. https://doi.org/10.1007/978-1-60761-444-9_5.

102. Wu, R., Dephoure, N., Haas, W., Huttlin, E.L., Zhai, B., Sowa, M.E., and Gygi, S.P. (2011). Correct interpretation of comprehensive phosphorylation dynamics requires normalization by protein expression changes. Mol. Cell. Proteomics *10*, M111.009654. https://doi.org/10.1074/mcp.M111.009654.

103. Kim, W., Bennett, E.J., Huttlin, E.L., Guo, A., Li, J., Possemato, A., Sowa, M.E., Rad, R., Rush, J., Comb, M.J., et al. (2011). Systematic and quantitative assessment of the ubiquitin-modified proteome. Mol. Cell *44*, 325–340. https://doi.org/10.1016/j.molcel.2011.08.025.

104. Huttlin, E.L., Jedrychowski, M.P., Elias, J.E., Goswami, T., Rad, R., Beausoleil, S.A., Villén, J., Haas, W., Sowa, M.E., and Gygi, S.P. (2010). A tissue-specific atlas of mouse protein phosphorylation and expression. Cell *143*, 1174–1189. https://doi.org/10.1016/j.cell.2010.12.001.

105. Käll, L., Canterbury, J.D., Weston, J., Noble, W.S., and MacCoss, M.J. (2007). Semi-supervised learning for peptide identification from shotgun proteomics datasets. Nat. Methods *4*, 923–925. https://doi.org/10.1038/nmeth1113.

106. Huang, D.W., Sherman, B.T., and Lempicki, R.A. (2009). Systematic and integrative analysis of large gene lists using DAVID bioinformatics resources. Nat. Protoc. *4*, 44–57. https://doi.org/10.1038/nprot.2008.211.

107. Stirling, D.R., Swain-Bowden, M.J., Lucas, A.M., Carpenter, A.E., Cimini, B.A., and Goodman, A. (2021). CellProfiler 4: improvements in speed, utility and usability. BMC Bioinf. *22*, 433. https://doi.org/10.1186/s12859-021-04344-9.

STAR★METHODS

KEY RESOURCES TABLE

REAGENT or RESOURCE	SOURCE	IDENTIFIER
Antibodies		
anti-CRTC2 (5B10) monoclonal Mouse	Cell Signaling Technology	13017, RRID:AB_2798088
anti-CRTC2 polyclonal Rabbit	Merck	ST1099, RRID:AB_2276561
anti-CRTC3 (EPR3440) monoclonal Rabbit	Abcam	ab91654, RRID:AB_2049542
anti-HA (6E2) monoclonal Mouse	Cell Signaling Technology	2367, RRID:AB_10691311
anti-HA monoclonal (Rabbit)	Cell Signaling Technology	3724, RRID:AB_1549585
anti-FLAG polyclonal Rabbit	Cell Signaling Technology	2368, RRID:AB_2217020
anti-COX2 (E7V6C) monoclonal Mouse	Cell Signaling Technology	37843, RRID:AB_3661723
anti-GAPDH monoclonal Mouse	Millipore	MAB374, RRID:AB_2107445
anti-MAVS polyclonal Rabbit	Cell Signaling Technology	3993, RRID:AB_823565
anti-STAT3 monoclonal Mouse (124H6)	Cell Signaling Technology	9139, RRID:AB_331757
anti-Phospho-STAT3 Y705 (D3A7)	Cell Signaling Technology	9145, RRID:AB_2491009
anti-Phospho-PKA substrate (100G7E) rabbit monoclonal	Cell Signaling Technology	9624, RRID:AB_331817
IRDye 800CW goat anti-mouse IgG	LI-COR	925–32210, RRID:AB_2687825
IRDye 800CW goat anti-rabbit IgG	LI-COR	925–32211, RRID:AB_2651127
IRDye 680RD goat anti-mouse IgG	LI-COR	925–68070, RRID:AB_2651128
IRDye 680RD goat anti-rabbit IgG	LI-COR	925–68071, RRID:AB_2721181
Anti-mouse IgG (H + L), F(ab')2 Fragment (Alexa Fluor® 488 Conjugate)	Cell Signaling Technology	4408S, RRID:AB_10694704
Goat anti-rabbit IgG Alexa Flour 568	Thermo Fisher Scientific	11011, RRID:AB_143157
anti-VACV polyclonal Rabbit	Abcam	AB35219, RRID:AB_778768
anti-Calnexin polyclonal Rabbit	LSBio	LS-B6881-100, RRID:AB_11186721
Bacterial and virus strains		
Sendai virus (Cantell strain)	ATCC	VR-907
Cytomegalovirus (Merlin strain)	Stanton et al.[82]	RCMV1111
Modified Vaccinia Ankara	Blanchard et al.[83]	MVA
Respiratory Syncytial Virus (Strain A2)	Gift from Dr Dalan Bailey	RSV
Herpes Simplex Virus 1 (KOS strain)	Nagel et al.[84]	HSV1
Stbl3 competent bacteria	ThermoFisher	C737303
E. coli. (α-Select Silver Competent Cells)	Bioline	BIO-85026
Chemicals, peptides, and recombinant proteins		
Diclofenac	MedChemExpress	HY-15036
H89	LKT laboratories	H0003
PGE2	Tocris biotechnology	2296
TransIT-293	Mirus Bio	MIR 2700
Lipofectamine 2000	Thermo	11668027
DharmaFECT 1	Horizon	T-2001-02
Tandem mass tag (TMT) 10-plex isobaric reagents	Thermo Fisher	90110
HPLC water	VWR	23595.328
LC-MS grade Acetonitrile	Merck	1.00029.2500
Formic acid	Thermo Fisher	85178
DTT	Sigma	43815-1G
Acetonitrile, Extra Dry	Thermo Scientific	AC364311000
Hydroxylamine	Sigma	438227

(*Continued on next page*)

Continued

REAGENT or RESOURCE	SOURCE	IDENTIFIER
Dulbecco's PBS	Sigma	D8537-500ML
DMEM	Sigma	D6429-500ML
Fetal Bovine Serum	Sigma	F7524-500ML
Trypsin-EDTA	Gibco	25300–054
Guanidine hydrochloride (8M)	Thermo Fisher	24115
DMSO	Sigma-Aldrich	D8418
Complete Protease Inhibitor Cocktail	Roche	11836153001
PhosSTOP Phosphatase inhibitor Tablets	Roche	4906845001
Fixation Buffer	BioLegend	420801
Nonidet P-40 (NP-40) substitute	Sigma-Aldrich	74385
Triton X-100	Sigma	X100-500ML
Glycerol	Sigma	G7757-1L
Sodium dodecyl sulfate	Fisher Chemical	S/P530/53
NotI	New England Biolabs	R0189S
XhoI	New England Biolabs	R0146S
Human Endothelial Serum Free Medium	Thermo	11111044
50xGibco™ Large Vessel Endothelial Supplement	Thermo	A14608-01
Keratinocyte SFM	Thermo	17005042
Polyinosinic-polycytidylic acid	Invivogen	tlrl-pic
Calf thymus DNA	Millipore	2618-250MG
Puromycin	Invivogen	ant-pr-1
Blasticidin	Invivogen	ant-bl-05
SpCas9 nuclease	Synthego	N/A
anti-HA agarose beads	Sigma	A2095-1ML
Iodoacetamide	Sigma-Aldrich	I1149-5G
Recombinant human IL-11	Biolegend	585902
Recombinant human IL-11RA	R&D Systems	8895-MR-050
Critical commercial assays		
IL-11 ELISA Kit	Abcam	ab100551
IL-11 ELISA Kit	R&D Systems	D1100
PGE2 ELISA Kit	R&D Systems	KGE004B
BCA Protein Assay Kit	Thermo Fisher	23227
Micro BCA Protein Assay Kit	Thermo Fisher	23235
QIAprep Spin Miniprep Kit	Qiagen	27104
QIAquick Gel Extraction Kit	Qiagen	28704
GoScript Reverse Transcriptase kit	Promega	A5001
Fast SYBR Green PCR Master Mix	Invitrogen	4385612
P3 primary cell 4D-Nucleofector X kit	Lonza	V4XP-3032
TURBO Dnase Kit	Thermo Fisher	AM2238
QIAGEN RNeasy	Qiagen	74104
QIAGEN Rnase-Free DNase Set	Qiagen	79254
Deposited data		
Mass spectrometry proteomics data	ProteomeXchange Consortium via the PRIDE partner repository	PXD051850
RNA sequencing raw data files (Sendai virus infection)	ArrayExpress database	E-MTAB-14001
RNA sequencing raw data files (IL-11 stimulation)	ArrayExpress database	E-MTAB-14684
Experimental models: Cell lines		
HFFF immortalized with human telomerase (HFFF-TERT)	Stanton et al.[85]	N/A
HEK293T	Gift from Prof. Paul Lehner	N/A

(*Continued on next page*)

Continued

REAGENT or RESOURCE	SOURCE	IDENTIFIER
A549	Gift from Prof. Paul Lehner	N/A
HUVEC/TERT-2	Gift from Dr. Jeanne Salje	N/A
HBEC3-KT	ATCC	CRL-4051
GGAGCGAGATCCCTCCAAAAT	Zhu et al.[86]	GADPH qPCR Forward
GGCTGTTGTCATACTTCTCATGG	Zhu et al.[86]	GADPH qPCR Reverse
ACCACTCTTCGGGAGAATACA	This Study	NR4A2 qPCR Forward
GGCATTTGGTACAAGCAAGGT	This Study	NR4A2 qPCR Reverse
GTGGCCAGATACAGCTGTCGC	Nishina et al.[87]	Il-11 qPCR Forward
GGTAGGACAGTAGGTCCGCTC	Nishina et al.[87]	Il-11 qPCR Reverse
GAAACCTCTTCCCGAAAGGAAA	Marentette et al.[88]	EP2 qPCR Forward
GACTGAACGCATTAGTCTCAGAA	Marentette et al.[88]	EP2 qPCR Reverse
CCGGCGGTGATGTTCATCTT	Yamamichi et al.[89]	EP4 qPCR Forward
CCCACATACCAGCGTGTAGAA	Yamamichi et al.[89]	EP4 qPCR Reverse
Further oligonucleotides	N/A	See Table S8
Recombinant DNA		
Gateway Control ("GAW")	This Study	N/A
HA-CRTC2	This Study	N/A
HA-CRTC2 dN50	This Study	N/A
CRTC3-HA-FLAG	This Study	N/A
CRTC3 dN50 - HA-FLAG	This Study	N/A
SIK2-HA-FLAG	This Study	N/A
Software and algorithms		
ImageJ	https://imagej.nih.gov/ij/	N/A
CellProfiler	https://cellprofiler.org/	N/A
ImageStudio	https://www.licor.com/bio/image-studio/	N/A
GraphPad Prism 9.3.1	https://www.graphpad.com/	N/A
BioRender	https://biorender.com/	N/A

EXPERIMENTAL MODEL AND SUBJECT DETAILS

Cells and cell culture

Human fetal foreskin fibroblast cells immortalised with human telomerase (HFFF-TERTs, male), HEK293T cells (female) and A549 cells (male) were grown in Dulbecco's modified Eagle's medium (DMEM) supplemented with fetal bovine serum (FBS: 10% v/v), and 100 IU/mL penicillin/0.1 mg/mL streptomycin (DMEM/FBS/PS) at 37°C in 5% v/v CO_2. HFFF-TERTs have been tested at regular intervals since isolation to confirm that human leukocyte antigen (HLA) and MHC Class I Polypeptide-Related Sequence A (MICA) genotypes, cell morphology and antibiotic resistance are unchanged. HEK293T cells were obtained as a gift from Professor Paul Lehner (Cambridge Institute for Therapeutic Immunology and Infectious Disease, Cambridge, UK) and had been authenticated by Short Tandem Repeat profiling.[90] A549 cells were isolated from the lung tissue of a white male with lung cancer. HBEC3-KT cells are a hTERT-immortalized lung epithelial cell line, isolated from the bronchus of a female patient. The cell line was acquired from ATCC (CRL-4051). HBEC3-KT cells were grown in Keratinocyte SFM (1X) complemented with 2.5 μg human recombinant epidermal growth factor (rEGF) and 25 mg bovine pituitary extract (BPE). HUVEC/TERT-2 cells (CRL-4053) are an hTERT-immortalized endothelial cell isolated from the vascular endothelium of a female patient. The cells were grown in Human Endothelial Serum Free Medium (SFM) supplemented with 50xGibco Large Vessel Endothelial Supplement (LVES). HUVEC/TERT 2 were a gift from Dr. Jeanne Salje (Cambridge Institute for Medical Research, Cambridge, UK), and were acquired from ATCC. All cells were confirmed to be Mycoplasma-negative (Lonza MycoAlert).

Viruses and cellular stimuli

Sendai virus (Cantell strain) was obtained from ATCC (VR-907). This strain is produced in embryonated eggs and produces a high proportion of 'defective interfering' genome intermediates in mammalian cells, and little to no productive virus. As such, viral effective titer was determined by the ability to cause IRF3 nuclear translocation for each batch, as 'MOI' is difficult to ascertain without a full

cycle of infection. A standard dilution of 1:100 Sendai virus to culture medium (2.5% FCS) was used for infections. After 2 h of infection, supernatant was removed and replaced with full culture medium (10% FCS).

The genome sequence of HCMV strain Merlin is designated the reference for HCMV by the National Center for Biotechnology Information, and was originally sequenced after 3 passages in human fibroblast cells.[91] A recombinant version (RCMV1111) of this strain was derived by transfection of a sequenced BAC clone.[82] RCMV1111 contains point mutations in two genes (RL13 and UL128) that enhance replication in fibroblasts.[82] Viral stocks were prepared from HFFF-TERTs as described previously.[85] When complete cytopathic effect was observed, cell culture supernatants were centrifuged to remove cell debris and then centrifuged at 22,000 × g for 2 h to pellet cell-free virus. The virus was resuspended in fresh DMEM, and residual debris was removed by centrifugation at 16,000 x g for 1 min.

Modified vaccinia Ankara (MVA) was obtained as a seed stock prepared from an original MVA stock at passage 575.[83] MVA was propagated in CEFs, purified by ultracentrifugation through two 36% (w/v) sucrose cushions and suspended in 10 mM Tris-HCl pH 9.0. MVA infectivity was determined by immunocytochemistry on CEFs and HFFF-TERTs cells, by using a polyclonal rabbit anti-VACV antibody.[92]

A fluorescent HSV-1 strain encoding UL47 with an in-frame C-terminal fusion to EYFP (A206K) was constructed using bacterial artificial chromosome (BAC)-cloned KOS strain of HSV-1.[93] Viral stocks were prepared in Vero cells and titrated using a plaque assay on HFFF-TERT monolayers. The RSV A2 strain that was used during this study was a kind gift from Dr Dalan Bailey (The Pirbright Institute, UK). Polyinosinic-polycytidylic acid (poly(I:C), Invivogen) was diluted in nuclease-free water (Ambion, ThermoFisher). Calf thymus DNA (CT-DNA) was purchased from Millipore, Merck, and diluted in nuclease-free water (Ambion, ThermoFisher). Both were transfected into the cytosol using lipofectamine 2000 or TransIT-LT1.

For IL-11 plus IL-11RA stimulation, HFFF-TERT cells were stimulated with 100 ng/ml IL-11 with 200 ng/ml IL-11RA in DMEM. Stimulation with IL-11 plus IL-11RA for RNAseq was for 24 h.

METHOD DETAILS

Plasmid construction

For exogenous gene expression, plasmids were constructed by either Gateway cloning into the a pHAGE vector under the control of an SFFV promoter,[18] or restriction enzyme cloning into a similar vector. The pDONR223 was employed as an entry clone as per the manufacturer's instructions, and as described in Nightingale et al.[18] A blasticidin S resistant pHAGE vector was constructed by subcloning the BSD gene in place of the parental pHAGE puromycin resistance gene. Construct sequences were validated by Sanger or Nanopore sequencing. Inserts were generated by PCR amplification from HFFF-TERT cDNA libraries or in the case of CRTC2 from a plasmid originating with the Harvard Medical School plasmid repository, and SIK2 from a plasmid originating with the MRC Protein Phosphorylation and Ubiquitylation Unit. The ΔN50 CRTC2 and ΔN50 CRTC3 constructs were created by PCR amplification from their respective wild-type parental plasmids.

Stable cell lines

Stable HFFF-TERT cell lines were generated by lentiviral transduction. HEK293T cells were transfected using TransIT293 as per the manufacturer's protocol with lentiviral vector, pCMV8.91 and VSVG expression plasmid. 48 h post transfection lentivirus containing supernatant was collected, and clarified by high speed centrifugation. Supernatant was then either used immediately or stored at −20°C for later use. Target HFFF-TERT cells were then transduced by application of lentivirus at a range of dilutions, and after approximately 72 h selected using 1μg/ml puromycin or 1μg/ml blasticidin as appropriate until control untransduced cells were all dead. Dilutions of lentivirus resulting in approximately 1/3 of cells surviving selection were taken forwards for experiments.

Immunoblotting

Cell samples were lysed in 1x RIPA buffer with protease inhibitors at 4°C. Lysates were clarified by centrifugation if required. Samples were mixed with 6x Laemmli buffer, boiled for 5 min then run on Biorad precast gels (4–15%) in 1x running buffer for 90 min at 100 V. Samples were then transferred to PVDF membrane at a constant 350mA for 1 h. Membranes were then blocked with 5% powdered milk solution in Tris-buffered saline with 0.1% Tween 20 detergent (TBST). Primary antibody incubations were routinely performed overnight at 4°C. After washing, LICOR secondary antibodies were added at 1:10,000 for 1 h while protected from light. Samples were washed again prior to imaging using a LICOR Odyssey CLx instrument.

Immunofluorescence

Cells were fixed using BD Cytofix fixation buffer as per the manufacturer's recommendations. Fixed cells were then washed in PBS and stored at 4°C until used. Cells were permeabilized using ice-cold methanol and then blocked in a solution of 2% FCS in PBS. Subsequent immunostaining was performed in a buffer of PBS, 2% FCS and 0.1% Tween 20 detergent. Cells were mounted in medium containing DAPI and either analyzed immediately or stored at 4°C until analyzed. Microscopy was performed on a Zeiss 710, EVOS cell imaging system or Zeiss 880. For endogenous CRTC2, the CST mouse monoclonal antibody was used. For endogenous CRTC3 the Abcam rabbit monoclonal antibody was used.

RNA extraction, cDNA and qPCR

RNA was extracted from 1-5x10^5 HFFF-TERT cells using the QIAGEN RNeasy kit as per the manufacturer's protocol. If the extracted RNA was to be used for RNAseq then as part of this protocol then DNA was digested on-column (QIAGEN RNase-Free DNase Set). If RNA was to be used for qPCR then DNase treatment was performed using Invitrogen TURBO DNase as per the manufacturer's protocol. Samples infected with Sendai virus for RNAseq were harvested at 8 h of infection.

cDNA was synthesised using Promega GoScript reverse transcriptase kit as per the manufacturer's instructions, following DNase treatment. Subsequent qPCR was performed using an applied biosystems Fast SYBR Green master mix system, and analyzed on a BioRad CFX touch thermocycler. Transcript expression was normalised to GAPDH, and analysis performed in BioRad CFX Maestro software, or by delta-Ct analysis in Microsoft Excel. Oligonucleotide sequences used are provided in Table S8.

Synthego Cas9/CRISPR

Guide RNA (gRNA) pools were purchased from Synthego as lyophilised RNA. These were resuspended in Tris-EDTA buffer before dilution in molecular biology grade water. gRNAs were then combined with an appropriate ratio of Cas9 protein and nucleofection supplement to form ribonucleoprotein complexes. 1.5x10^5 HFFF-TERT cells were nucleofected per reaction, using the Lonza 4D-X core unit. Single cell clones were isolated by limiting dilution and knockout verified by Western blot.

Drugs & Ligands

PGE2 was obtained from Tocris biotechnology (#2296) and resuspended in sterile DMSO. PGE2 was used in experiments at 20μM. Diclofenac was obtained from MedChemExpress (#HY-15036) and resuspended in sterile DMSO. Diclofenac was used in experiments at 20μM. H89 was obtained from LKT laboratories (H0003) and resuspended in sterile DMSO. H89 was used in experiments at 20μM.

For experiments in which drugs were applied during Sendai virus infection, to minimise the risk of interference with cellular entry of the virus, infection was first allowed to occur for 2 h. Media were then changed to include this indicated drugs for the remainder of the infection.

Immunoprecipitation

HFFF-TERT cells were transduced to express SIK2-HA-FLAG. Approximately 6x10^5 cells were infected with Sendai virus as described above. At 2 h post infection cells were returned to full medium, and 20μM diclofenac added to the medium where required. After a total of 24 h of infection cells were washed in ice-cold PBS. After lysis in 'lysis buffer' (50mM Tris-HCl pH7.4, 150mM NaCl, 5% glycerol, 1% NP-40, 0.1mM EDTA with phosphatase and protease inhibitors) for 30 min on ice, lysates were cleared by centrifugation, and the supernatant applied to pre-washed anti-HA agarose beads. Beads and lysate were incubated overnight at 4°C. Beads were then washed in lysis buffer four times, and bound protein eluted by boiling in an equal volume of 2x SDS loading buffer.

siRNAs

siRNA pools were obtained from Dharmacon as ON-TARGET plus siRNA SMARTpools (CRTC2: L-018947-00-0005; CRTC3: L-014210-01-0005; MAVS: L-024237-00-0005; COX2 (PTGS2): L-004557-00-0005; EP2 (PTGER2): L-005712-00-0005; EP4 (PTGER4): L-005714-00-0005; Non-targeting Control Pool: D-001810-10-05), resuspended as per the manufacturer's instructions, and stored in aliquots at −80°C. HFFF-TERT cells were seeded the day before siRNA transfection. The next day siRNAs were transfected using the transfection reagent DharmaFECT 1 as per the manufacturer's instructions. A final concentration of 50nM for each siRNA was used.

ELISA

Indicated cells were infected with Sendai virus for 24 h prior to supernatant harvest. Supernatants were clarified of any cellular debris by centrifugation prior to storage in aliquots at −80°C. Supernatants were thawed only once then discarded. Anti-IL11 ELISA assays were performed using either Abcam (ab100551) or R&D (D1100) kits as per the manufacturer's instructions. PGE2 ELISA assays were performed using the kit produced by R&D (KGE004B) as per the manufacturer's instructions. Colorimetric readings were measured using a Tecan spark platform.

RNAseq

poly(A) selective mRNA 3′ end sequencing libraries was prepared using QuantSeq 3′ mRNA-Seq Library Prep Kit-FWD (Lexogen). Libraries were sequenced by Cambridge Genomic Services. Reads were first trimmed to remove adaptors using BBDuk,[94] before alignment to concatenated human (GRCh38) and SeV (GenBank: AB855653) genomes using STAR.[95] Reads aligning to annotated genes were counted using HTSeq[96] and genes with fewer than 10 counts were excluded from downstream analysis. Normalisation and differential expression analysis was then performed using edgeR.[97]

Subcellular fractionation

HFFF-TERT cells were first either infected with Sendai virus or mock treated. At 8 h post infection cells were washed in PBS, then incubated with hypotonic lysis buffer (25mM Tris-HCl pH 7.5, 50mM Sucrose, 0.5mM MgCl2, 0.2mM EGTA). Cells were harvested

after incubation by scraping, and then lysed using a Dounce homogeniser. Following lysis, sucrose concentration was immediately adjusted to physiological osmolarity by addition of an appropriate volume of hypertonic sucrose buffer (25mM Tris-HCl pH 7.5, 2.5M Sucrose, 0.5mM MgCl2, 0.2mM EGTA). The nuclear fraction was then isolated by centrifugation at 1,000g for 10 min, and the post-nuclear lysate was centrifuged at 78,400g for 30 min. The resulting pellet represents the organellar fraction, and the supernatant the cytosolic fraction. Nuclear and organellar fractions were resuspended in Guanidine-HEPES buffer (6M Guanidine/50 mM HEPES pH 8.5). The cytosolic fraction was concentrated by Trichloro-acetic acid (TCA) precipitation. Briefly, 100% TCA was added to cytosol sample in a 1:5 ratio and incubated at 4°C. The sample was then centrifuged at 21,000g for 30 min at 4°C. Protein pellets were then washed in TCA and then acetone before resuspension in Guanidine-HEPES buffer.

Subcellular fractions in Guanidine-HEPES buffer were further processed by reduction by dithiothreitol (DTT) at a final concentration of 5mM, then alkylated using iodoacetamide (15mM final concentration). Excess iodoacetamide was then quenched with an excess of DTT. Samples were then diluted with 200mM HEPES pH 8.5 to a final guanidine concentration of 1.5M. Proteins were then digested with LysC protease at a 1:100 protease: protein ratio. Following LysC digest, samples were further diluted in 200mM HEPES to a final guanidine concentration of 0.5M. Samples were then digested with Trypsin at a 1:100 protease: protein ratio overnight at 37°C. The next day the reaction was quenched by the addition of formic acid to a volume of 5%, centrifuged to remove undigested protein, and peptides processed by C18 solid-phase extraction (SPE, Sep-Pak, Waters) and vacuum-centrifuged to near-dryness.

Whole cell lysate protein digestion for proteomics

Cells were washed twice with phosphate buffered saline (PBS), and 250 μL Guanidine-HEPES buffer added (6M Guanidine/50 mM HEPES pH 8.5). Cell lifters (Corning) were used to scrape cells in lysis buffer, which was removed to an Eppendorf tube, vortexed extensively then sonicated. Cell debris was removed by centrifuging at 21,000 g for 10 min twice. Dithiothreitol (DTT) was added to half of the sample to a final concentration of 5mM and incubated at room temperature for 20 min. Cysteine residues were alkylated with 15 mM iodoacetamide and incubated for 20 min at room temperature in the dark. Excess iodoacetamide was quenched with DTT for 15 min. Samples were diluted with 200 mM HEPES pH 8.5 to 1.5 M Guanidine followed by digestion at room temperature for 3 h with LysC protease at a 1:100 protease-to-protein ratio. Samples were further diluted with 200mM HEPES pH8.5 to 0.5 M Guanidine. Trypsin was then added at a 1:100 protease-to-protein ratio followed by overnight incubation at 37°C. The reaction was quenched with 5% formic acid and centrifuged at 21,000 g for 10 min to remove undigested protein. Peptides were subjected to C18 solid-phase extraction (SPE, Sep-Pak, Waters) and vacuum-centrifuged to near-dryness.

Peptide labeling with tandem mass tags (TMT)

In preparation for TMT labeling, desalted peptides were dissolved in 200mM HEPES pH8.5. TMT reagents were dissolved in anhydrous acetonitrile and 3 μL added to peptide at a final acetonitrile concentration of 30% (v/v). Details of TMT labeling are given in Table S7. Following incubation at room temperature for 1 h, the reaction was quenched with hydroxylamine to a final concentration of 0.3% (v/v). TMT-labelled samples were combined at a 1:1:1:1:1:1 (subcellular fractionation) or 1:1:1:1:1:1:1:1:1:1 (whole cell lysate) ratio. The sample was vacuum-centrifuged to near dryness and subjected to C18 SPE (Sep-Pak, Waters). An unfractionated single shot was analyzed initially to ensure similar peptide loading across each TMT channel, thus avoiding the need for excessive electronic normalization.

Offline HpRP fractionation

TMT-labelled tryptic peptides were subjected to HpRP fractionation using an Ultimate 3000 RSLC UHPLC system (Thermo Fisher Scientific) equipped with a 2.1 mm internal diameter (ID) x 25 cm long, 1.7 μm particle Kinetix Evo C18 column (Phenomenex). Mobile phase consisted of A: 3% acetonitrile (MeCN), B: MeCN and C: 200 mM ammonium formate pH 10. Isocratic conditions were 90% A/10% C, and C was maintained at 10% throughout the gradient elution. Separations were conducted at 45°C. Samples were loaded at 200 μL/min for 5 min. The flow rate was then increased to 400 μL/min over 5 min, after which the gradient elution proceed as follows: 0–19% B over 10 min, 19–34% B over 14.25 min, 34–50% B over 8.75 min, followed by a 10 minuteswash at 90% B. UV absorbance was monitored at 280 nm and 15 s fractions were collected into 96 well microplates using the integrated fraction collector. Fractions were recombined orthogonally in a checkerboard fashion, combining alternate wells from each column of the plate into a single fraction, and commencing combination of adjacent fractions in alternating rows. Wells were excluded prior to the start or after the cessation of elution of peptide-rich fractions, as identified from the UV trace.

LC-MS3

MS data were generated using an Orbitrap Fusion Lumos (Thermo). An Ultimate 3000 RSLC UHPLC machine equipped with a 300 μm internal diameter × 5 mm Acclaim PepMap μ-Precolumn (Thermo) and a 75 μm internal dimeter × 50 cm 2.1 μm particle Acclaim PepMap RSLC analytical column were used. The loading solvent was 0.1% FA. The analytical solvent consisted of 0.1% FA (A) and 80% AcN +0.1% FA (B). All separations were carried out at 40°C. Samples were loaded at 5 μL/min for 5 min in loading solvent. The analytical gradient consisted of 3–7% B over 3 min, 7–37% B over 173 min, followed by a 4 min wash at 95% B and equilibration at 3% B for 15 min. Each analysis used a MultiNotch MS3-based TMT method.[98] The following settings were used: MS1: 380–1500 Th, 120,000 resolution, 2×10^5 automatic gain control (AGC) target, 50 ms maximum injection time. MS2: Quadrupole isolation at an isolation width of mass-to-charge ratio (m/z) 0.7, collision-induced dissociation fragmentation (normalized collision

energy (NCE) 35) with ion trap scanning in turbo mode from m/z 120, 1.5×10^4 AGC target, 120 ms maximum injection time. MS3: In Synchronous Precursor Selection mode, the top 10 MS2 ions were selected for higher energy collision dissociation (HCD) fragmentation (NCE 65) and scanned in the Orbitrap at 60,000 resolution with an AGC target of 1×10^5 and a maximum accumulation time of 150 ms. Ions were not accumulated for all parallelisable time. The entire MS/MS/MS cycle had a target time of 3 s. Dynamic exclusion was set to ±10 ppm for 70 s. MS2 fragmentation was triggered on precursors 5×10^3 counts and above.

QUANTIFICATION AND STATISTICAL ANALYSIS

Proteomic data analysis

In the following description, the first report in the literature for each relevant algorithm is listed. Mass spectra were processed using MassPike, which is a Sequest-based software pipeline for quantitative proteomics, through a collaborative arrangement with Professor Steven Gygi's laboratory at Harvard Medical School. MS spectra were converted to mzXML using an extractor built upon Thermo Fisher's RAW File Reader library (version 4.0.26). This software is a component of the MassPike software platform and is licensed by Harvard Medical School.

A combined database was constructed as described in[18] from (a) the human Uniprot database (accessed 26 January 2017), (b) all Sendai virus proteins (c) common contaminants such as porcine trypsin and endoproteinase LysC. The combined database was concatenated with a reverse database composed of all protein sequences in reversed order. Searches were performed using a 20 ppm precursor ion tolerance.[99] Product ion tolerance was set to 0.03 Th. Oxidation of methionine residues (15.99492 Da) was set as a variable modification. Peptides were assumed to be fully tryptic with up to two missed cleavages.

To control the fraction of erroneous protein identifications, a target-decoy strategy was employed.[100,101] Peptide spectral matches (PSMs) were filtered to an initial peptide-level false discovery rate (FDR) of 1% with subsequent filtering to attain a final protein-level FDR of 1%.[102,103] PSM filtering was performed using linear discriminant analysis as described previously.[104] Filtering was implemented in R using the linear discriminant analysis (LDA) function in the package MASS (cran.r-project.org/web/packages/MASS). This distinguishes correct from incorrect peptide identifications in a manner analogous to the widely used Percolator algorithm[105] although employing a distinct machine-learning algorithm. The following parameters were considered: XCorr, ΔCn, missed cleavages, peptide length, charge state, and precursor mass accuracy. Peptides shorter than seven amino acids in length or with XCorr less than 1.0 were excluded prior to LDA filtering.

Protein assembly was guided by principles of parsimony to produce the smallest set of proteins necessary to account for all observed peptides (algorithm described in.[104] Proteins were quantified by summing TMT reporter ion counts across all matching peptide-spectral matches using "MassPike", as described previously.[98] Briefly, a 0.003 Th window around the theoretical m/z of each reporter ion was scanned for ions and the maximum intensity nearest to the theoretical m/z was used. The primary determinant of quantitation quality is the number of TMT reporter ions detected in each MS3 spectrum, which is directly proportional to the signal-to-noise (S:N) ratio observed for each ion. An isolation specificity filter with a cut-off of 50% was additionally employed to minimise peptide co-isolation.[98] Peptide-spectral matches with poor quality MS3 spectra (a combined S:N ratio of less than 250 across all TMT reporter ions) or no MS3 spectra at all were excluded from quantitation. Peptides meeting the stated criteria for reliable quantitation were then summed by parent protein, in effect weighting the contributions of individual peptides to the total protein signal based on their individual TMT reporter ion yields. Protein quantitation values were exported for further analysis in Excel.

For protein quantitation, reverse and contaminant proteins were removed, then each reporter ion channel was summed across all quantified proteins and normalised assuming equal protein loading across all channels. For further analysis and display in Figures, fractional TMT signals were used (i.e., reporting the fraction of maximal signal observed for each protein in each TMT channel, rather than the absolute normalized signal intensity). This effectively corrected for differences in the numbers of peptides observed per protein.

Pathway analysis

The Database for Annotation, Visualisation and Integrated Discovery (DAVID) was used to determine functional enrichment.[106] A given cluster was always searched against a background of all proteins or transcripts quantified.

Cellprofiler

A nuclear:cytosolic fluorescence ratio was quantified using a custom pipeline in Cellprofiler.[107] In brief, nuclei were defined on the basis of the area covered by DAPI staining, and a mask created based on this region. Nuclei touching the edge of the field of view were excluded. To measure the cytoplasmic fluorescence intensity the area of the nuclear mask was extended by 10 pixels, then the area covered by the nuclear mask was subtracted. The remaining area was defined as the cytosol. This approach was chosen as opposed to attempting to quantify the entire cytosol to compensate for differences in cell shape, size and crowding. The nuclear:cytosplasmic ratio was then calculated for each nucleus by dividing the mean fluorescence of each nucleus by the mean fluorescence of the associated cytosolic field.

To access the statistical significance of the conditions quantified on CellProfiller, two-tailed *p*-values using the non-parametric Mann-Whitney test were calculated using Graphpad Prism 9.3.1. The Pearson correlation coefficient (r) and 95% confidence intervals were estimated using Graphpad Prism 9.3.1.

Sequence alignment

53 promoter sequences were enriched in the RNA-Seq dataset comparing CRTC2/3 DKO HFFF-TERTs complemented either with CRTC2+CRTC3 or control then infected with Sendai virus. The sequences were aligned using the Clustal Omega (https://www.ebi.ac.uk/jdispatcher/msa/clustalo) tool for multiple sequence alignments. The resulting alignment was upload to WebLogo 2.8.2 (https://weblogo.berkeley.edu/) to generate the sequence logo based on the base conservation and frequency.

Statistical analysis of qPCR and ELISA data

The exact n for each experiment is in the respective figure legend. For pairwise comparisons, unless otherwise specified, unpaired two-tailed t-tests were employed. Where comparing to data normalised to 1 (for example Figure S5A), a one sample t test was performed. Significance levels denoted by asterisks are specified in the figure legends.